High–pressure (P= 1.5 – 1.8 GPa) blueschist from Elba: implications for underthrusting and exhumation of continental units in the Northern Apennines.

Samuele PAPESCHI[a*], Giovanni MUSUMECI[a,b], Hans-Joachim MASSONNE[c,d], Francesco MAZZARINI[b], Eric RYAN[e] and Giulio VIOLA[f]

a. Dipartimento di Scienze della Terra, Università di Pisa, via Santa Maria 53, 56126 Pisa, Italy

b. Istituto Nazionale di Geofisica e Vulcanologia, via della Faggiola 32, 56126 Pisa, Italy

c. School of Earth Sciences, China University of Geosciences, 388 Lumo Road, 430074 Wuhan, P.R. China

d. Fakultät Chemie, Universität Stuttgart, Pfaffenwaldring 55, D-70569 Stuttgart, Germany

e. Department of Geoscience and Petroleum, Norwegian University of Science and Technology, Sem Sælands veg 1, N-7491 Trondheim, Norway

f. Dipartimento di Scienze Biologiche, Geologiche e Ambientali, Università di Bologna, via Zamboni 67, 40126 Bologna, Italy

***Corresponding author:**

Primary e-mail: s.papeschi@gmail.com

Institutional e-mail: samuele.papeschi@unifi.it

Phone: +393202472057

Address: Dipartimento di Scienze della Terra, via Santa Maria 53, 56126 Pisa (PI), Italy.

This article has been accepted for publication and undergone full peer review but has not been through the copyediting, typesetting, pagination and proofreading process, which may lead to differences between this version and the Version of Record. Please cite this article as doi: 10.1111/jmg.12530

Authors' details

Samuele Papeschi; samuele.papeschi@unifi.it **ORCID** 0000-0002-5774-7119

Giovanni Musumeci; giovanni.musumeci@unipi.it **ORCID** 0000-0001-5343-4708

Hans-Joachim Massonne; h-j.massonne@mineralogie.uni-stuttgart.de **ORCID** 0000-0002-2826-4767

Francesco Mazzarini; francesco.mazzarini@ingv.it **ORCID** 0000-0002-3864-6558

Eric Ryan; eric.j.ryan@ntnu.no

Giulio Viola; giulio.viola3@unibo.it **ORCID** 0000-0002-8383-3328

Abstract

The Acquadolce subunit on the Island of Elba, Italy, records blueschist-facies metamorphism related to the Oligocene-Early Miocene stages of continental collision in the Northern Apennines. The blueschist-facies metamorphism is represented by glaucophane- and lawsonite-bearing metabasite associated with marble and calcschist. These rock types occur as lenses in a schistose complex representing foredeep deposits of early Oligocene age. Detailed petrological analyses on metabasic and metapelitic protoliths, involving mineral and bulk-rock chemistry coupled with P–T and P–T–X(Fe_2O_3) pseudosection modelling using PERPLE_X, show that the Acquadolce subunit recorded nearly isothermal exhumation from peak pressure–temperature conditions of 1.5–1.8 GPa and 320–370 °C. During exhumation, peak lawsonite- and possibly carpholite- or stilpnomelane-bearing assemblages were overprinted and partially obliterated by epidote-blueschist and, subsequently, albite-greenschist facies metamorphic assemblages. This study sheds new light on the tectonic evolution of Adria-derived metamorphic units in the Northern Apennines, by showing (1) the deep underthrusting of continental crust during continental collision, and (2) rapid exhumation along 'cold' and nearly isothermal paths, compatible with syn-orogenic extrusion.

Keywords: blueschist; glaucophane; lawsonite; continental underthrusting; syn-orogenic extrusion.

1. Introduction

High-pressure–low-temperature (HP–LT) rocks are commonly found in suture zones of orogenic belts, recording early subduction of oceanic crust before initial continental collision (e.g. Miyashiro, 1961; Honegger, Le Fort, Mascle, & Zimmermann, 1989; Liou, Wang, Coleman, Zhang, & Maruyama, 1989). Exhumed blueschist- and eclogite-facies rocks, found in orogens, not only represent markers of subduction processes and related metamorphism, but also store information on the tectonometamorphic evolution of orogenic wedges and the recycling of crustal material at convergent margins (e.g. Ernst, 1973, 1988, 2001; Platt, 1993; Maruyama, Liou, & Terabayashi, 1996; Stern, 2005; Angiboust, Agard, Raimbourg, Yamato, & Huet, 2011; Tsujimori & Ernst, 2014). Petrological and geochronological investigations of HP–LT rocks can shed light on the pressure–temperature–time path experienced during oceanic subduction or early continental collision (e.g.

Davis & Whitney, 2006; Warren & Waters, 2006; Kryza, Willner, Massonne, Muszyński, & Schertl, 2011; Vitale Brovarone et al., 2011; Aoya, Endo, Mizukami, & Wallis, 2013; López-Carmona, Pitra, & Abati, 2013; López-Carmona, Abati, Pitra, & Lee, 2014), and are hence invaluable for understanding the exhumation and tectonic processes that are active in past and present orogenic belts (Platt, 1993; Maruyama et al., 1996; Ring, Brandon, Willett, & Lister, 1999; Ring & Glodny, 2010; Searle & Lamont, 2020).

In the Aegean area, for instance, detailed metamorphic petrology and geochronology of the Cycladic Blueschist Units, has demonstrated the importance of extrusion tectonics during exhumation of deep-seated HP–LT rocks (Ring & Layer, 2003; Jolivet & Brun, 2010; Ring & Glodny, 2010; Searle & Lamont, 2020). Syn-orogenic extrusion has been proposed also for the northern Tyrrhenian Sea (e.g. Jolivet et al., 1998), where the pioneering works of Theye, Reinhardt, Goffe, Jolivet, & Brunet, (1997), Giorgetti, Goffe, Memmi, & Nieto, (1998), and Rossetti et al. (1999) revealed the existence of exhumed continental and oceanic HP–LT rocks, related to early Apenninic continental collision (Rossetti, Glodny, Theye, & Maggi, 2015). In spite of this evidence, exhumation of HP–LT rocks in the Northern Apennines has been ascribed by many authors to be a result of post-orogenic extension (e.g. Carmignani & Kligfield, 1990; Carmignani et al., 1994; Brogi, 2008), mostly because of the present-day setting of the northern Tyrrhenian Sea within an area of active crustal thinning (Cassinis, Scarascia, Lozej, & Finetti, 2005; Pondrelli et al., 2006).

In this contribution, we present a case study of blueschist-facies metabasites and associated calcschists and metapelites from the Island of Elba (Italy) that record early continental collision and exhumation of continental crust in the Northern Apennines. A detailed petrographic and mineralogical description of the investigated rocks is presented and is integrated with the modeled mineral chemistry obtained by pressure–temperature (P–T) and P–T–X pseudosection calculations, to constrain peak and retrograde metamorphism. The P–T path, reconstructed from different rock types, allowed us to reconstruct the evolution of the investigated units in the geodynamic framework of the Northern Apennines–Alps orogenic system, and to shed new light on the exhumation of HP–LT units in the Northern Apennines, before crustal extension.

2. Geological Outline

2.1 The Northern Apennines–Corsica orogenic system

The Alps and the Apennines are two oppositely-verging orogenic systems, formed after 90 Ma of convergence between the Adria microplate and the European margin, leading to the complete subduction of the Alpine Tethys Ocean (Figure 1a; Elter, Elter, Sturani, & Weidmann, 1966; Boccaletti, Elter, & Guazzone, 1971). The Alpine system, exposed on the Island of Corsica, is separated from the Northern Apennines by the Northern Tyrrhenian Sea, which has classically been interpreted as a Late Miocene back-arc basin (Jolivet et al., 1998; Brunet, Monié, Jolivet, & Cadet, 2000). The European Variscan basement of Corsica is overlain on the northeastern sector of the island (Alpine Corsica) by W-verging (1) continental Europe-derived units, (2) ocean-derived units (Schistes Lustrés), accreted during the Late Cretaceous–Eocene period, and (3) the so-called Nappes Supérieures (upper units), consisting of non-metamorphic ophiolitic and continental units (Figure 1a; Durand-Delga, 1984; Malavieille, Chemenda, & Larroque, 1998). Eocene HP–LT parageneses are found in the entire Alpine Corsica nappe stack, except for the uppermost unit (Balagne-Nebbio Unit; Caron, 1994; Daniel, Jolivet, Goffe, & Poinssot, 1996; Tribuzio & Giacomini, 2002; Chopin, Beyssac, Bernard, & Malavieille, 2008; Vitale Brovarone et al., 2013; Vitale Brovarone & Herwartz, 2013). On the opposite side of the Northern Tyrrhenian Sea, the Northern Apennines are characterized by NE-verging nappes that were accreted during the subduction of the Adria microplate from the Oligocene to the present-day (Figure 1a; Boccaletti et al., 1971; Elter, 1975). The Northern Apennine nappe stack comprises, from top to bottom: (1) the Ligurian and Subligurian Units, oceanic and ocean–continent transition nappes containing Jurassic ophiolite sequences and their Jurassic–Paleocene cover with associated flysch deposits; (2) several Adria-derived nappes, notably the Tuscan Nappe in the hinterland sector and the Cervarola–Falterona Unit and Umbria–Marche Units in the external part of the belt, characterized by carbonate-dominated Triassic–Paleogene passive margin sequences capped by Oligocene–Miocene foredeep deposits; (3) a group of metamorphic nappes, collectively referred to as the Tuscan Metamorphic Units (TMUs), that comprise a Paleozoic Variscan basement overlain by fragments of a Carboniferous–Oligocene sedimentary cover, which is correlated to that of the Tuscan Nappe. The nappe stack is covered by Neogene–Quaternary wedge-top deposits and was affected by Late Miocene–Quaternary intrusive and extrusive arc magmatism, dominated by anatectic melts of crustal signature (Serri, Innocenti, & Manetti, 1993).

Contrary to Alpine Corsica, the Northern Apennines nappe stack is dominated by non-metamorphic to subgreenschist facies units (e.g. Franceschelli, Leoni, Memmi, & Puxeddu, 1986). The Ligurian Units, representing the non-metamorphic analogue of the Schistes Lustrés, generally escaped HP–LT subduction-related metamorphism and remained at upper crustal levels. Sodic amphibole-bearing Ligurian Units are only found in the Monte Argentario area (P–T ≥ 0.7 GPa at ~340 °C; Theye et al., 1997) and in the Island of Giglio (P–T = 0.7–0.8 GPa at 300–350 °C; Biancone & Tucci, 1984; Rossetti et al., 1999). The Island of Gorgona, in the middle of the Northern Tyrrhenian Sea, is characterized by blueschist-facies metaophiolites, which were interpreted to belong to the Schistes Lustrés. P–T conditions of 1.3–1.6 GPa at 300–350 °C were estimated for these rocks (Jolivet et al., 1998), which were dated at 25.6±0.3 Ma using the $^{40}Ar/^{39}Ar$ system on phengite (Brunet et al., 2000). As for Adria-derived units, greenschist- to blueschist-facies parageneses occur only in the TMUs. Typical chloritoid-bearing assemblages have been reported in the Apuan Alps (P–T ranging from 0.4–0.6 GPa at 360–420 °C to 0.6–0.8 GPa at 420–500 °C; Jolivet et al., 1998; Molli, Giorgetti, & Meccheri, 2000; Molli, Vitale Brovarone, Beyssac, & Cinquini, 2018) and the Monti Pisani (P–T = 0.8–0.9 GPa at ~475 °C; Lo Pò & Braga, 2014). Similar or higher pressures were estimated for the carpholite-bearing Monticiano-Roccastrada Unit (P–T = 0.6–0.8 to ~1.1 GPa at 340–370 to 370–420 °C; Giorgetti et al., 1998; Brogi & Giorgetti, 2012), Monte Argentario (P–T = 0.8–1.0 GPa at 350–420 °C; Theye et al., 1997) and the Island of Giglio (P–T = 1.2–1.4 GPa at 310–350 °C; Rossetti et al., 1999). Geochronological estimates for peak metamorphism in the TMUs, obtained via $^{40}Ar/^{39}Ar$ on phengite, range between ~27 Ma (Apuan Alps; Kligfield, Hunziker, Dallmeyer, & Schamel, 1986) and 16.2±0.3 Ma (Argentario; Brunet et al., 2000). Blueschist-facies rocks were recently found also on the eastern part of the Island of Elba (Bianco et al., 2015), and are described in detail in the following section.

The Northern Apennines are thought to have experienced Oligocene continental collision, followed by Late Miocene to present slab roll-back that caused extension in the upper plate hinterland sector and migration of the 'contractional front' towards the foreland in the East (Malinverno & Ryan, 1986; Carmignani et al., 1994 and references therein). More recently, studies on sedimentary basins, syntectonic intrusions, and fault systems have shown that episodic Late Miocene shortening transiently interrupted extensional tectonics in the hinterland sector of the Northern Apennines

(Bonini et al., 2014; Musumeci, Mazzarini, & Cruden, 2015; Viola et al., 2018 and references therein). In this framework, contrasting and often composite models explain the exhumation of the metamorphic units either as a result of syn-orogenic extrusion (Storti, 1995; Jolivet et al., 1998; Rossetti, Faccenna, Jolivet, Goffé, & Funiciello, 2002; Molli, 2008; Molli et al., 2018), post-orogenic extension (Carmignani & Kligfield, 1990; Carmignani et al., 1994), or basement thrusting (Carosi, Montomoli, & Pertusati, 2004; Balestrieri, Pandeli, Bigazzi, Carosi, & Montomoli, 2011; Bonini et al., 2014).

2.2 Geology of the Island of Elba

The structure of the Island of Elba is characterized by N–S trending, E-verging nappes stacked by W-dipping thrusts that developed largely between the Early Miocene and the Pliocene (Figure 1b; Pertusati, Raggi, Ricci, Duranti, & Palmeri, 1993; Keller & Coward, 1996; Massa, Musumeci, Mazzarini, & Pieruccioni, 2017; Viola et al., 2018). Early Miocene thrusting was followed by Middle Miocene synorogenic extension and exhumation of metamorphic units and then by a renewed top-to-the-ENE Late Miocene–Early Pliocene contractional phase, coeval with the emplacement of magmatic rocks (Musumeci et al., 2015; Massa et al., 2017; Papeschi, Musumeci, & Mazzarini, 2017; Viola et al., 2018). In this framework, the Zuccale Fault, previously interpreted as an extensional detachment (e.g. Collettini & Holdsworth, 2004), has been reinterpreted as an Early Pliocene out-of-sequence thrust (Musumeci et al., 2015; Viola et al., 2018).

The Late Miocene Capo Norsi–Monte Arco thrust divides the nappe stack into an Upper Complex and a Lower Complex (Figure 1b). From top to bottom, the Upper Complex consists of three Ligurian-derived units (the Cretaceous Flysch Unit, the Paleogene Flysch Unit, and the ophiolite-bearing Ligurian Unit) that overlie the Adria-derived Tuscan Nappe and the greenschist-facies Rio Marina Unit, containing Carboniferous–Triassic basement rocks. The Lower Complex comprises two basement-and-cover metamorphic units that are part of the TMUs: the greenschist- to blueschist-facies Ortano Unit and the amphibolite-facies Calamita Unit at the base of the nappe stack. A slice of strongly tectonized serpentinite, originally part of the Ligurian Unit, is sandwiched between the Rio Marina Unit and the Lower Complex, and smeared along the Capo Norsi–Monte Arco thrust (Massa et al., 2017; Serpentinite Unit in Figure 1b). The nappe stack is intruded by several Late

Miocene intrusives. The Monte Capanne pluton (between 7.007±0.007 and 7.323±0.019 Ma; ID-TIMS U/Pb youngest zircon ages; Barboni, Annen, & Shoene, 2015) intruded the Ligurian Unit on Western Elba (Figure 1b); the Central Elba laccolith complex (between 7.437±0.011 and 7.942±0.008 Ma; ID-TIMS U/Pb youngest zircon ages; Barboni et al., 2015) consists of sheets of different magmas that were emplaced in the Cretaceous Flysch Unit and the Ligurian Unit (Figure 1b; Dini, Innocenti, Rocchi, Tonarini, & Westerman, 2002). The Porto Azzurro pluton intruded the Calamita Unit (Lower Complex) in Eastern Elba (Figure 1b; Barberi, Innocenti, & Ricci, 1967a; Musumeci & Vaselli, 2012). Since most of the Porto Azzurro pluton is buried below the sea level, age constraints were obtained only from outcropping tourmaline-rich apophyses (5.9±0.2 Ma; $^{40}Ar/^{39}Ar$ biotite age; Maineri et al., 2003), and leucogranitic dykes (6.33±0.07 Ma; $^{40}Ar/^{39}Ar$ biotite age; Musumeci et al., 2015), both likely representing late magmatic manifestations. The intrusion of the Porto Azzurro pluton resulted in large-scale low-pressure–high-temperature (LP–HT) metamorphism in the Lower Complex, completely obliterating the regional metamorphic assemblage in the Calamita Unit and, partially, also in the southern part of the Ortano Unit.

LP–HT metamorphism occurred at $P < 0.2$ GPa reaching peak temperatures of 600–700 °C in the Calamita Unit and 450–600 °C in the Ortano Unit (Duranti, Palmeri, Pertusati, & Ricci, 1992; Musumeci & Vaselli, 2012; Papeschi, Musumeci, Massonne, Bartoli, & Cesare, 2019). Available radiometric ages on the LP–HT assemblage constrain contact metamorphism between 6.76±0.08 Ma ($^{40}Ar/^{39}Ar$ phlogopite age) and 6.23±0.06 Ma ($^{40}Ar/^{39}Ar$ muscovite age), corroborated by a 6.40±0.15 Ma U/Pb zircon age (Musumeci, Mazzarini, Tiepolo, & Di Vincenzo, 2011; Musumeci et al., 2015).

Blueschist- to greenschist-facies parageneses (Bianco et al., 2015) are preserved in the Ortano Unit (Acquadolce subunit; Massa et al., 2017), north of Mt. Fico, where the effect of LP–HT metamorphism already dissipated along strike towards the North (Figure 1b, 2). Bianco et al. (2015) reported the occurrence of glaucophane-bearing lenses of metabasite, with a chemical composition transitional between tholeiitic basalt and alkali basalt, enveloped within foliated marble and phyllite. Lawsonite pseudomorphs, enclosed in epidote and albite, were later documented by Bianco et al. (2019). Based on the content of the glaucophane end-member in amphibole and the jadeite end-member in pyroxene, Bianco et al. (2015) estimated peak P–T conditions around 0.9–1.0 GPa and 330–350 °C. Later on, Bianco et al. (2019) suggested peak pressures likely above 1.5 GPa. However,

detailed P–T estimates were hindered by inhomogeneous metamorphism of the investigated rocks. $^{40}Ar/^{39}Ar$ dating on phengite from the schistose rocks associated with the metabasite yielded a 19.68±0.15 Ma plateau age (Deino, Keller, Minelli, & Pialli, 1992), coeval with the 19.8 ± 1.4 Ma $^{40}Ar/^{39}Ar$ glaucophane age obtained by Bianco et al. (2019) (location in Figure 2).

2.3 Acquadolce subunit: geological outline

The Ortano Unit (Figure 2) is characterized by a Middle Ordovician basement (Ortano porphyroid; Musumeci et al., 2011), overlain by Jurassic marble (Ortano marble) and a complex of schist and metapsammite, containing lenses of marble, cherty marble, and calcschist, known as the Acquadolce subunit (Massa et al., 2017). Metabasite bodies occur disseminated in the lower part of the Acquadolce subunit, included within metacarbonates (Figure 2). Throughout the Ortano Unit, the metamorphic foliation strikes approximately N–S and dips gently to moderately (10–50°) to the W (Figure 2).

The Acquadolce subunit is separated from the rest of the Ortano Unit by the Late Miocene Felciaio Shear Zone (FSZ; Figure 2), which was active during peak LP–HT metamorphism associated with the emplacement of the Porto Azzurro pluton in eastern Elba (Musumeci & Vaselli, 2012). For this reason, while the Ortano marble and the Ortano porphyroid experienced amphibolite-facies metamorphism at $P < 0.2$ GPa (Duranti et al., 1992), the effect of the LP–HT imprint on the Acquadolce subunit caused only the development of cordierite- and andalusite-bearing spotted schists, mainly in the southern part of the area (south of M. Fico–Punta dell'Acquadolce; Figure 2). The northern part of the Acquadolce subunit largely escaped Late Miocene LP–HT metamorphism and preserves blueschist-facies parageneses, mostly in metabasite lenses (Bianco et al., 2015) with T/E MORB geochemical affinity (Bianco et al., 2019). Contact metamorphic parageneses in metapelites, calcschists, and metabasites are only represented by the incipient growth of biotite (Rio Marina–S. Filomena area), and of plagioclase, which forms a rim around pure albite cores (from Punta dell'Acquadolce to the South; Figure 2; Table S1 in supplementary material).

The age and paleogeographic attribution of the Acquadolce subunit are in part unclear. Detrital zircon dating indicates an Early Oligocene minimum deposition age at least for the schistose rocks of the Acquadolce subunit occurring at the top of the sequence in the Ortano valley (Jacobs et al., 2018;

sample location in Figure 2), whereas the marble, calcschist and metabasite lenses were ascribed to the Cretaceous by Duranti et al. (1992). Recently, Massa et al. (2017) correlated the Acquadolce subunit with the younger formations of the Tuscan Nappe (i.e. Cretaceous–Oligocene Scaglia Toscana Fm.).

3. Blueschist-facies metabasite and associated lithologies

The metabasite bodies of the Acquadolce subunit occur in scattered outcrops, exposed along the coastline between Rio Marina and Punta dell'Acquadolce (Figure 2). The relationship with the host rocks is well exposed at Rio Marina (Torretta di Rio Marina outcrop) and has been summarized in the lithostratigraphic column in Figure 3a. At this location, metabasite occurs as lens-shaped bodies, hosted in metacarbonates, with thickness between some decimeters and 1–2 meters (Figure 3a). The dominant mafic rock type is dark to light green (Figure 3b) and contains a very fine-grained amphibole + chlorite + epidote matrix which surrounds millimetric porphyroclasts of clinopyroxene and whitish albite aggregates. The structure of the metabasite varies from poorly-foliated or granofelsic (e.g. Figure 3b) to well-foliated, showing continuous variation even through single layers (e.g. Figure 3c). The foliation in the metabasite is defined mostly by the preferred orientation of chlorite and amphibole. Close to the contact with the surrounding carbonates, the foliation is finely layered (few centimeters in thickness); however, in general, the metabasite shows a spaced foliation, surrounding rock portions lacking a discernable orientation. Metabasite layers commonly exhibit symmetric boudinage structures with carbonate + epidote-rich veins in necks between boudins, nearly perpendicular to the foliation.

The host of the metabasite is made up of relatively pure mylonitic marble (gray to white in color) and impure light-green mylonitic calcschist (Figure 3a). As shown in Figure 3a and Figure 3b, at the Torretta di Rio Marina outcrop, the mylonitic calcschist layers are commonly found within a few decimeters from the contact with the metabasite, generally interleaved with millimetric to centimetric lenses of amphibole + chlorite-rich metabasic material (Figure 3d). The green color of the mylonitic calcschist is largely related to the presence of chlorite, epidote, amphibole, and white mica. These minerals occur either as grains dispersed throughout the carbonatic matrix or enriched in fine-grained lenses/layers of green-colored schists (Figure 4a). Millimeter-sized white albite grains are

visible at the mesoscale within the mylonitic calcschists (Figure 4a). The mylonitic marble, away from the metabasite lenses, contains mm-thick metapelitic layers mainly consisting of white mica, chlorite, and albite.

The transition from the metabasite lenses to the host carbonate is marked by a sharp increase in foliation intensity (Figure 4b). There is a single, continuous (mylonitic) schistosity in the carbonates, defined by the preferred orientation of mineral grains and by intercalations of thin layers of phyllosilicate-rich material, stretched along the foliation (Figure 4b). Both blueschist- (i.e. amphibole) and greenschist-facies minerals appear strongly oriented along this foliation, indicating a strong reorganization of the peak fabric during retrograde deformation.

The foliation is also folded around tight to isoclinal sheath folds (Figure 4c), associated with constantly E–W to NE–SW trending stretching lineation (Figure 4d), defined by oriented aggregates of carbonates, trails of chlorite-white mica, and oriented amphibole grains.

4. Petrography

Microstructures and metamorphic parageneses of the Acquadolce subunit have been investigated in a suite of samples (see Table S1 in the supplementary material), the location and names of which are reported in Figure 2. The samples are registered on SESAR and additional details (lithological description, GPS coordinates and microphotographs) are available at https://app.geosamples.org/. Oriented thin sections were prepared and cut parallel to the lineation and perpendicular to the foliation. Petrographic investigations with the optical microscope were coupled with preliminary analysis of the mineral chemistry using a ZEISS-EVO SEM equipped with an Oxford Instruments EDS detector at the National Institute for Geophysics and Volcanology (Pisa, Italy) and a Hitachi TM3030 Plus Tabletop Microscope SEM at the Department of Earth Sciences (University of Pisa).

We selected a sample of metabasite (IESP3SP56; foliation oriented dip/dip-direction: 28/308) and a sample of calcschist (IESP3SP53; 26/320) for detailed petrographic and mineral chemistry studies. The selected samples, collected 50 cm apart, are from metabasite and calcschist layers in contact at the Torretta di Rio Marina outcrop (Figure 3a, 3b), and are those that best preserve the peak blueschist-facies assemblage among all the investigated samples and show only a weak contact metamorphic imprint.

4.1 Metabasite

The metabasite contains, with decreasing modal content, amphibole + chlorite + clinopyroxene + epidote + albite + titanite + quartz + calcite. The microstructures of this rock are characterized by large, brownish clinopyroxene porphyroclasts (grain size: 0.2–2 mm), surrounded by a green to blue matrix made up of fine-grained amphibole + chlorite + epidote + quartz (grain size: 2–5 μm–100 μm) (Figure 5a). Clinopyroxene porphyroclasts are partially replaced by very fine-grained intergrowths of chlorite + titanite + albite + quartz + amphibole, the latter also occurring in strain shadows around or in fractures within the porphyroclasts (Figure 5b). The prismatic shape of clinopyroxene, only locally preserved (Figure 5a), suggests that these porphyroclasts were originally primary constituents of the igneous protolith, in agreement with Bianco et al. (2015). However, SEM-EDS analyses carried out during this work and microprobe analyses reported by Bianco et al. (2015, 2019) reveal an omphacitic composition, demonstrating re-equilibration during blueschist-facies metamorphism.

The foliation is heterogeneous and very poorly developed, and is mostly defined by the preferred orientation of amphibole and chlorite grains (Figure 5a). Unfoliated domains are characterized by irregular patches of epidote, titanite, albite, and quartz.

Amphibole is zoned, showing a dark to lavender blue Na-rich core (Na-amphibole), surrounded by a pale green rim of Ca-amphibole (Figure 5c). Na-amphibole is commonly associated with clinopyroxene porphyroclasts (Figure 5b) and forms acicular to prismatic (~ 0.1–1 mm grain size) grains in the matrix (Figure 5c). Ca-amphibole forms a thin, euhedral rim around Na-amphibole grains as well as tiny, acicular grains (~ 10–50 μm) localized in the chlorite-rich matrix (Figure 5c). Epidote grains have euhedral to anhedral habits, ranging in size from 2–5 μm to about 100 μm (Figure 5d). In general, epidote is zoned and characterized by a relatively Fe-poor core (clinozoisite) surrounded by a 'pistacitic' Fe-rich rim (e.g. Figure S5 in supplementary material). However, epidote grains with complex zoning patterns are also present. Pseudomorphs of rhomboedral lawsonite grains (~10–100 μm grain size) occur in the matrix, and as inclusions in epidote and albite (Figure 5e). Lawsonite has been replaced by aggregates of clinozoisite-epidote, and quartz (Figure 5e; concentration maps of major elements are available in Figure S6 and S7 in the supplementary material), as also reported by Bianco et al. (2019). Albite forms irregular patches, roughly 50–100 μm

across, displaying a strongly lobate shape at the contact with partially-resorbed Na-amphibole grains and sharp, straight boundaries at the contact with Ca-amphibole, epidote, and titanite grains (Figure 5f). Titanite occurs as euhedral grains and clusters, ranging in size from 5–10 μm up to 200 μm (e.g. Figure 5f). Quartz and chlorite grains are distributed in the matrix (Figure 5d, e, f). Calcite grains locally occur in clusters but are the major component of veins crosscutting the sample.

To summarize, it is possible to distinguish an early metamorphic assemblage, documented by relic lawsonite, Na-amphibole, clinozoisite, and clinopyroxene, from a later overprinting assemblage of albite + Ca-amphibole + Fe-epidote + chlorite + titanite + quartz. The relic mineral assemblage can be further subdivided into an earlier stage with lawsonite formation and a later stage when lawsonite was pseudomorphosed by clinozoisite. Na-amphibole is inferred to have been present during both stages.

4.2 Calcschist

The calcschist consists of 80–90 % calcite (estimated on thin sections with ImageJ), organized in layers ranging in thickness between some hundreds of micrometers and the millimeter. Other mineral phases (given in decreasing modal content) are chlorite, white mica, albite, epidote, Na-amphibole, titanite, quartz, and accessory apatite, rutile, zircon, and tourmaline (in modal order). The non-carbonatic phases are concentrated in thin (10–20 μm, up to 100–200 μm) lepidoblastic layers, defining the main metamorphic foliation of the sample (Figure 6a). Chlorite, white mica, and Na-amphibole share a common shape preferred orientation in these layers (Figure 6a). Subparallel white mica and chlorite also occur as single grains within calcite layers, defining the foliation therein (Figure 6a, b). Stacks of chlorite and white mica, intricately intergrown and oriented at high angle to the foliation in local crenulations, are also present (Figure 6c).

The calcite grains are 1–3 mm across with amoeboid shapes and lobate grain boundaries, that contain deformed mechanical twins and bands of smaller, recrystallized grains (grain size: 20–100 μm) with granoblastic microstructure (Figure 6b). The preferred orientation of both large calcite grains and bands of recrystallized grains contributes to define the foliation within calcite-rich domains (Figure 6b).

The grain size of chlorite and white mica varies generally between 5 and 50 μm. Na-amphibole grains (grain size: 0.1–1.0 mm) display prismatic to fish-shaped habits and commonly contain inclusions of quartz, calcite, rutile, and apatite. Na-amphibole is very commonly boudinaged along the main foliation, with calcite + quartz located interstitially between boudins (Figure 6d). Epidote (grain size: 10–200 μm) forms euhedral grains, localized in the chlorite + white mica-rich matrix (Figure 6d, e). As shown in Figure 6e, epidote can contain allanite cores with oscillatory zoning, interpreted as detrital cores (see also Figure S15, S17).

Albite is present as large porphyroclasts (up to 1–2 mm), synkinematic with respect to the main foliation, containing poikiloblastic inclusions of calcite, quartz, epidote, Na-amphibole, white mica, chlorite, and titanite (Figure 6f). Na-amphibole within albite is partially resorbed, whereas titanite and epidote are in textural equilibrium with albite (Figure 6g). Small albite rims are also commonly present around Na-amphibole grains (e.g. Figure 6h). Very tiny quartz grains and aggregates, commonly organized in very thin layers (< 10–50 μm thickness), are dispersed within the chlorite + white mica matrix (e.g. Figure 6e, h). Titanite (grain size: 10–100 μm), apatite, and zircon (grain size: 5–50 μm) commonly display euhedral shapes (e.g. Figure 6e). Titanite commonly contains poikiloblastic inclusions of quartz and rutile (e.g. Figure 6e). The few rutile grains present in the matrix (grain size: 10–50 μm) are preserved as anhedral aggregates partially overgrown by titanite (Figure 6e, h). Thus, rutile was probably stable at peak conditions.

Based on microstructural relationships, the peak mineral assemblage, represented by Na-amphibole + rutile + quartz, was overprinted by albite + epidote + titanite + quartz. Matrix white mica and chlorite are interpreted as being present throughout the metamorphic evolution of the investigated calcschists, since they occur also in stacks crosscut by the main foliation (Figure 6c).

5. Mineral chemistry

The chemical composition of minerals in the selected samples was determined using a CAMECA SX100 electron microprobe (EMP) equipped with five WDS spectrometers and an EDS system at the Institut für Mineralogie und Kristallchemie (Universität Stuttgart). Analytical conditions for spot analyses were 15 kV accelerating voltage, 15 nA beam current, 20 s counting time on peak and background each, and 1 μm spot size. The standards used were wollastonite (Si, Ca), Al_2O_3 (Al),

Fe_2O_3 (Fe), $MnTiO_3$ (Mn, Ti), albite (Na), orthoclase (K), olivine (Mg) and barite (Ba). Structural formulae of minerals were recalculated considering 14 oxygen equivalents for chlorite, 11 for white mica, 23 for amphibole, 12.5 for epidote, 8 for feldspar, 5 for titanite, and 4 for rutile. The Fe^{3+} content of amphibole was recalculated using PROBE-AMPH (Tindle & Webb, 1994) and MINCALC-V5 (Bernhardt, 2007).

Na- and Ca-amphibole were classified using the classification scheme by Deer, Howie, & Zussman (1992), and white mica based on the Al^{VI}–Al^{IV} diagram by Bousquet, Goffé, Vidal, Oberhänsli, & Patriat (2002). Concentration maps for major elements (Ca, Fe, Mn, Mg, Al, Na) were also produced by stepwise movements of the thin section under the electron beam; counting times per step were 100 ms. Representative mineral analyses are shown in Tables 1 and 2. All analyses, and their location, are available in the supplementary material to this article (Section S1–S2–S3–S4 in the supplementary material).

5.1 Metabasite

The amphibole composition is highly variable from Na-amphibole in the core to Ca-amphibole (actinolite) in the rim (Figure 7a). Na-amphibole shows a wide chemical variability from 'crossite' to glaucophane (Figure 7b) with Si = 7.76–7.97 per formula unit (p.f.u.), X_{Mg} (= Mg p.f.u./[Fe + Mg p.f.u.]) = 0.52–0.65, and X_{Na} (= Na p.f.u./[Na+K+Ca p.f.u.]) = 0.86–0.98. 'Crossite' was analyzed mainly in the core, whereas glaucophane occurs closer to the rim (Table 1). The chemical variation of the actinolitic rim is characterized by Si = 7.66–7.95 p.f.u., Ca = 1.69–1.85 p.f.u., X_{Mg} = 0.63–0.78, and Na = 0.11–0.33 p.f.u. The calculated X_{Fe}* = Fe^{2+} p.f.u./(Fe^{2+}+Fe^{3+} p.f.u.) increases from 0.36–0.75 in the Na-amphibole core to 0.66–0.90 in the actinolitic rim, accompanying the increase in X_{Mg}. In all amphiboles, K, Ti, and Mn content proportions are always near zero (below 0.02–0.03 p.f.u.; Table 1).

Clinozoisite-epidote generally displays direct zoning with Fe^{3+} = 0.0–0.4 p.f.u. in the core to Fe^{3+} = 0.4–0.9 p.f.u. in the rim (Figure 7c). However, some grains are characterized by complex intergrowths of Fe^{3+}-poor and Fe^{3+}-rich clinozoisite-epidote. K, Na, Ti, Mg, and Mn contents are close to zero in all the analyzed epidote grains. Chlorite displays Si = 2.80–3.00 p.f.u., Al = 2.22–2.34 p.f.u., and X_{Fe} (= Fe p.f.u./[Fe + Mg p.f.u.]) = 0.26–0.34 (Figure 7d). Albite is nearly pure in

composition with Ca < 0.01 p.f.u. and K close to zero (Table 1). Titanite contains 0.5–1.5% wt% Al_2O_3 (Table 1). The major potassium-bearing phase in the sample is phengitic white mica that occurs, intergrown with chlorite, in clinopyroxene pseudomorphs. Analyses of phengite were all poor because of the very fine grain size. No preserved relics of clinopyroxene and lawsonite were found in this study.

5.2 Calcschist

Chlorite, white mica, epidote, and albite in the calcschist are relatively homogeneous in composition (see below), whereas Na-amphibole displays concentric zoning from core to rim (Figure 8a), related to a sharp increase in Mg (Figure 8b) and, in particular, Mn (Figure 8c) towards the rim, accompanied by a very slight increase in Na (Figure 8d) and a decrease in Fe. Mn is also heterogeneously distributed in chlorite, with local, relatively high peaks observed in some grains (Figure 8b).

The composition of Na-amphibole ranges from 'crossite' in the core to glaucophane in the rim (Figure 9a). The zoning from crossite to glaucophane is accompanied by an increase in X_{Mg} from 0.49 to 0.66 (Figure 9b), in Al from 0.62 to 1.64 p.f.u., and in MnO from nearly zero to 0.08 p.f.u. (Figure 9c). The MnO content ranges from 0.10–0.20 (core) to 0.45–0.65 wt% (rim) (Table 2). X_{Fe}* increases from roughly 0.40–0.64 (core) to 0.59–0.65 in the rim (Table 2). White mica is phengitic, halfway between the muscovite and celadonite end-members, and seems to display a certain solid-solution towards a trioctahedral mica component (Figure 9d). As the extent of this miscibility clearly exceeds that experimentally found by Massonne & Schreyer (1986), we interpret the observed composition as contamination by intergrown chlorite (e.g. Figure 6c). The composition of phengite is largely Si = 3.45–3.51 p.f.u., X_{Fe} = 0.26–0.33 (Figure 9e), and X_{Na} < 0.03. Chlorite is characterized by Si = 2.83–3.04 p.f.u., Al = 2.20–2.30 p.f.u., X_{Fe} = 0.28–0.31 (Figure 9f), and MnO contents between 0.2 and 1.1 wt% (Table 2).

Epidote compositions are close to the pistacite end-member, $Ca_2Al_2Fe^{3+}Si_3O_{12}(OH)$, with Al = 1.87–2.10 p.f.u. and K, Na, Ti, Mg, and Mn contents close to zero (Table 2). The allanitic cores of epidote show oscillatory zoning with La_2O_3, Ce_2O_3, and Y_2O_3 contents between 0.5 and 10.2 wt%, 0.1 and 5.7 wt%, and 0 and 0.7 wt%, respectively (Table 2). Albite is pure with Ca and K contents close to zero. Titanite displays Al_2O_3 contents consistently near ~ 1 wt% (Table 2).

6. Pseudosection modeling

The bulk-rock chemistry of samples IESP3SP53 (calcschist) and IESP3SP56 (metabasite) was determined by X-ray fluorescence spectroscopy (XRF) using a Panalytical PW2400 spectrometer at the Institut für Mineralogie und Kristallchemie at Universität Stuttgart. The carbonate fraction of the ground sample IESP3SP53 was previously removed by reaction with diluted HCl, based on the lack of microstructural evidence of metamorphic reactions between the silicate and carbonate minerals (more details below). FeO (and Fe_2O_3) was analyzed by wet chemical titration at the Università di Padova, Italy. The bulk composition of the samples (shown as wt% in Table 3) was recalculated to fit the $MnO–Na_2O–CaO–K_2O–FeO–MgO–Al_2O_3–SiO_2–H_2O–TiO_2–O_2$ (MnNCKFMASHTO) system, used for pseudosection modeling (Table 3). In particular, P_2O_5 was fractionated as apatite, together with corresponding amounts of CaO.

Pseudosections were calculated using PERPLE_X 6.8.6 (Connolly, 2005, 2009) and the hp02ver.dat thermodynamic dataset (Holland & Powell, 2001; Connolly & Kerrick, 2002). The solution models used were: Gt(HP)–garnet, St(HP)–staurolite, Ctd(HP)–chloritoid, Pheng(HP)–phengitic mica, Ep(HP)–epidote, Omph(HP)–clinopyroxene, Chl(HP)–chlorite (Holland & Powell, 1998), Mica(M)–paragonitic mica, Stlp(M)–stilpnomelane (Massonne, 2010), Opx(HP)–orthopyroxene (Powell & Holland, 1999), MtUl(A)–magnetite (Andersen & Lindsley, 1988), feldspar–ternary feldspar (Fuhrman & Lindsley, 1988), Bio(TCC)–biotite (Tajčmanová, Connolly, & Cesare, 2009) and the ideal IlGkPy–ilmenite, Carp–carpholite, hCrd–cordierite, and T–talc models. The low-temperature amphibole models Namph(M) (Kryza et al., 2011), Act(M) (Massonne & Willner, 2008), and GlTrTsMr (Liu et al., 2009) were tested in different pseudosections. Namph(M) considers the compositional variability of sodic amphibole in the tremolite–glaucophane–riebeckite–Mg-riebeckite space, Act(M) in the tremolite–actinolite–glaucophane–Mg-riebeckite space, and GlTrTsMr in the glaucophane–tremolite–tschermakite–Mg-riebeckite space. The fluid phase was taken as pure H_2O, and set in excess, based on the extensive presence of epidote in both samples, which is stable only at very low values of X_{CO2} (= CO_2 mol%/[CO_2+H_2O mol%]) in a hydrous fluid (see Bucher-Nurminen, Frank, & Frey, 1983 and Bucher & Grapes, 2011). The inferred presence of substantial lawsonite at peak conditions in the metabasite, also implies that water was in excess (see

Clarke, Powell, & Fitzherbert, 2006). Additionally, we tested the effect of X_{CO2} on the stability of amphibole and epidote in preliminary P–X_{CO2} pseudosections at T = 300, 350 and 400 °C (those for T =350 °C are reported in Figure S21, S22 in supplementary material). Epidote, amphibole, lawsonite, and titanite are stable for X_{CO2} < 0.01–0.05 in the 0.2–2.2 GPa pressure range, thus validating our assumption of a virtually CO_2-free fluid.

6.1 Metabasite

A first-order limitation for pseudosection modeling in the metabasite sample is represented by the wide chemical and textural variability of the observed mineral phases (amphibole and epidote for instance; Figure 7), which suggests that the rock is characterized by grain-scale disequilibria and element partitioning that make thermodynamic modelling using pseudosections challenging. In any case, we tentatively calculated P–T pseudosections to obtain insights into the metamorphic evolution of the metabasites.

In order to describe in detail the mineralogical variability of Na- and Ca-amphibole in the sample, we calculated two P–T pseudosections for the P–T range 0.2–1.4 GPa and 300–500 °C using either Namph(M) (Figure 10a and simplified version in Figure 10b) or Act(M) (Figure 10c and simplified version in Figure 10d). The GlTrTsMr model, which was used in preliminary pseudosections, is not suitable for the here relevant low-temperature amphiboles, as it predicts significant proportions of the tschermak component even for T < 400 °C.

The phase diagrams calculated with either Namph(M) or Act(M) are fairly similar in first order (Figure 10b, d). Considering the T = 300–400 °C temperature interval, both diagrams predict lawsonite + amphibole occurring at P > 0.9–1.2 GPa, epidote + amphibole at P = 0.5–1.2 GPa, and albite + epidote below 0.5–1.2 GPa, whereas garnet-bearing fields occur at higher temperatures, above 380–420 °C (Figure 10b, d). The main differences regard the P–T fields of amphibole, omphacite, and paragonite.

The Namph(M) model, for instance, limits the P–T field of amphibole to blueschist-facies conditions (plagioclase-free fields; Figure 10b). In most of the plagioclase-bearing fields, biotite appears as Fe–Mg-bearing phase (Figure 10a). On the other hand, the Act(M) model stabilizes amphibole in most of the greenschist-facies fields (Figure 10d) and limits the biotite-bearing fields to

higher temperatures (Figure 10d). This is not surprising since Namph(M) considers only tremolite Ca-amphibole end-members that would be stable at greenschist-facies conditions (e.g. Bucher & Grapes, 2011), whereas an additional Ca-amphibole end-member is included in Act(M). The composition of amphibole, calculated with Namph(M), is characterized by a high proportion of glaucophane component for most of the blueschist-facies, and an increase in the riebeckite component towards the lawsonite- and the plagioclase-bearing fields (Figure 10a). These compositions are comparable to those observed for Na-amphiboles in the sample (Figure 7b). However, X_{Gl} is always > 0.55 and 'true' Ca-amphiboles never appear (Figure 10a). Differently, the Act(M) model predicts amphibole compositions with low $X_{Na} < 0.6$ for pressures between 0.6 and 1.0 GPa and 'true' sodic compositions never appear, even at P > 1.0–1.4 GPa (Figure 10c). Another direct consequence of the choice of the models is that omphacite is stable at epidote-blueschist-facies conditions with Namph(M) (Figure 10b), while Act(M) stabilizes paragonite towards higher pressures (Figure 10d). The change in the modes of these phases can be seen in Figure 11 along modal profiles calculated at T = 350 °C and varying pressure. They predict similar modal proportions of epidote, chlorite, quartz, albite, titanite, phengite, rutile, and biotite. The modes of albite and epidote approach zero towards the greenschist-blueschist facies and the epidote-blueschist to lawsonite-blueschist facies transition respectively. Instead of epidote, lawsonite appears as a major constituent with a ~20% modal proportion (Figure 11a, b). In both cases, the disappearance of albite is accompanied by a strong increase in amphibole and paragonite. Around 9% of paragonite is predicted using the Namph(M) model (Figure 11a), whereas this percentage increases to around 20% using Act(M) in the epidote-blueschist facies (Figure 11b). On the other hand, only a very small proportion of omphacite appears using the Namph(M) (Figure 11a). In any case, clinopyroxene does not occur or in very small modal proportions in the calculated pseudosections. This is consistent with the textural evidence of amphibole, chlorite, and epidote, overgrowing clinopyroxene, which is very likely an igneous relic (Figure 5b). The local omphacitic pyroxene spectrum (Figure S6), also reported by Bianco et al. (2015, 2019), might be to some extent the result of local equilibria. Finally, we note that the use of Namph(M) results in higher proportions of stilpnomelane towards high pressure (up to 12%; Figure 11a), compared to the Act(M) model (Figure 11b).

Taking into account the limitations of the solid-solution models, Namph(M) can be tentatively used to describe the variability of glaucophane–crossite amphibole in the blueschist-facies, whereas Act(M) can be used to constrain the actinolite–tremolite amphibole at greenschist-facies conditions. Considering the phase diagram calculated with Namph(M), lawsonite is stable in the presence of Na-amphibole beyond 0.7–1.3 GPa in the 300–400 °C temperature range (Figure 10a). Many lawsonite-bearing P–T fields are also characterized by rutile as part of the assemblage, which was not observed. The pseudomorphing of lawsonite by epidote and quartz can be related to the transition from the lawsonite- to the epidote-bearing fields during the P–T evolution of the sample. The assemblage epidote + phengite + Na-amphibole + chlorite + titanite + quartz is stable together with paragonite and omphacite over a wide range of P–T conditions between 0.6 and 1.3 GPa and 300 and 470 °C (Figure 10a). Paragonite, which was not found in the sample, was likely obliterated by retrograde metamorphism, notably by the growth of albite. The stability field of garnet provides an upper temperature limit at T = 400–500 °C at P = 1.0–1.4 GPa. The wide chemical variability of Na-amphibole suggests that this mineral continuously grew over a wide range of P–T conditions, likely in the lawsonite- to epidote-bearing fields, hindering the possibility to precisely link Na-amphibole growth to a particular P–T range. We tentatively plotted isopleths for the X_{Fe} content of chlorite in the phase diagram calculated with Namph(M) (Figure 10a); however, the observed X_{Fe} range of chlorite (0.26–0.34) is predicted to be stable at 0.5–0.9 GPa at the transition from plagioclase-absent to plagioclase-bearing fields. Hence, chlorite likely re-equilibrated during retrograde metamorphism (Figure 10a).

The greenschist-facies assemblage epidote + phengite + plagioclase (albite) + Ca-amphibole + chlorite + titanite + quartz occurs at P = 0.2–0.8 GPa and T = 300–420 °C (Figure 10c). At higher temperature, biotite, rutile, and hematite join the mineral assemblage at the expense of titanite and phengite.

Based on the modeled mineral assemblage and mineral chemistry, it is not possible to precisely constrain the P–T path of the metabasite. The preserved paragenesis suggests, however, a progressive evolution from early, blueschist-facies metamorphism (lawsonite- to epidote-blueschist facies) to later, greenschist-facies metamorphism. The lack of garnet indicates a maximum

metamorphic temperature of 380–420 °C. The former presence of lawsonite suggests a peak pressure above 0.8–1.3 GPa.

6.2 Calcschist

As a first approach, we calculated a preliminary H_2O-saturated P–T phase diagram in the P–T range of 0.2–2.2 GPa at 300–600 °C using the analyzed bulk-rock composition and the FeO–Fe_2O_3 content obtained by wet chemical titration (Figure S23 in supplementary material). Since this sample is characterized only by Na-amphibole, we used the Namph(M) to model this phase. In the calculated diagram, quartz is stable across the entire P–T range and titanite is present at T < 420 °C and P < 0.8 GPa, while rutile occurs at higher pressures and temperatures. Na-amphibole occurs in all plagioclase-absent P–T fields and, in the presence of albitic plagioclase, in a restricted P–T range between 0.2 and 0.6 GPa and 300 and 400 °C. Garnet appears in the HP–HT part of the diagram (red line in S23, above 0.6–1.4 GPa at 360–540 °C), whereas phengite is present in all P–T fields except at LP–HT conditions (yellow line in Figure S23; beyond ~480 °C at 0.2–1.6 GPa). However, low modal contents (<1–2 vol.%) of hematite, which was not observed, occur in most of the fields, coexisting with rutile or titanite. This indicates that the chosen Fe_2O_3 content, obtained by wet chemical titration, is too high, probably due to late oxidation of the rock.

Therefore, we calculated a series of P–X pseudosections at fixed temperature (T = 300, 350 and 400 °C) for the 0.6–2.0 GPa pressure range and $X(Fe^{3+}) = Fe^2O^3/(FeO + Fe_2O_3)$ between 0 (i.e. all Fe considered divalent) and 0.48 (i.e. value obtained by wet chemical titration) to constrain an appropriate $X(Fe^{3+})$ value for this sample. Temperatures above 400 °C are unlikely because the preliminary diagram predicts garnet to be stable in most of the lawsonite-bearing fields for T > 360–420 °C (Figure S23). We used the composition of phengite, in terms of X_{Fe} and Si p.f.u., to quantitatively constrain the P–T conditions of equilibration of the investigated sample. Phengite is, indeed, characterized in the rock by a very narrow compositional range with Si = 3.45–3.51 p.f.u. and X_{Fe} = 0.26–0.33 (Figure 9e).

As shown in Figure 12 for 350 °C, hematite is stable for $X(Fe^{3+})$ between 0.4 and 0.5, whereas rutile and titanite appear for $X(Fe^{3+})$ < 0.4 above and below P = 1.0–1.2 GPa, respectively. The observed phengite Si p.f.u. and X_{Fe} isopleths intersect in the phengite + amphibole + stilpnomelane +

paragonite + chlorite + lawsonite + quartz + rutile field, for a restricted X(Fe^{3+}) range between 0.05 and 0.15. At this interval and in the pressure range 0.6–2.0 GPa, rutile is the stable Ti phase, whereas titanite occurs at lower pressures (hematite is absent). A similar X(Fe^{3+}) range was estimated from the analysis of the pseudosections calculated for other temperatures than 350 °C. Therefore, we calculated several P–T pseudosections for X(Fe^{3+}) = 0.05, 0.10, and 0.15. In Figure 13a, we show the pseudosection corresponding to X(Fe^{3+}) = 0.10, while a simplified version is presented in Figure 13b.

In this diagram, garnet appears in the presence of lawsonite above 360–420 °C (Figure 13a, b). Na-amphibole occurs in the plagioclase- and garnet-absent fields for P above 0.6–0.8 GPa and T below 360–460 °C. Rutile is present above 1.0–1.2 GPa in the lawsonite field, whereas titanite is the predominant Ti phase in the epidote- + Na-amphibole-bearing fields and in the presence of plagioclase (Figure 13a, b). Excluding garnet-bearing fields, the calculated phengite isopleths intersect for Si p.f.u. = 3.45–3.50 and XFe = 0.26–0.32 in the P = 1.5–1.8 GPa and T = 320–370 °C range (violet shaded field in Figure 13a). At such conditions, the metamorphic assemblage is phengite + Na-amphibole + stilpnomelane + paragonite + chlorite + lawsonite + quartz + rutile, and even carpholite for P > 1.6–1.8 GPa. At slightly higher temperatures (330–390 °C), the assemblage consists of phengite + amphibole + paragonite + chlorite + lawsonite + quartz + rutile (Figure 13a). As shown in the modal profile at T = 350 °C in Figure 13c, the sample should have contained non-negligible modal proportions of lawsonite (7–11%), stilpnomelane (up to 3%), and paragonite (1–3%) in the 1.5–1.7 GPa pressure range. Moreover, for P around 1.8 GPa, up to 25% of stilpnomelane, and up to 15% of carpholite should have been present (Figure 13c). The presence of lawsonite pseudomorphs in the associated metabasite (see Figure 5e and Bianco et al., 2019) suggests that lawsonite was probably also present in the calcschist. Another indication of the former presence of lawsonite is provided by the glaucophane-rich amphibole rim, which, according to pseudosection modeling, is predicted to be stable at P > 1.0–1.4 GPa, chiefly in the lawsonite- and rutile-bearing fields. Similarly, any former paragonite might have been consumed during the retrograde path during the growth of other Na-bearing phases (i.e. albite). The Mn-enrichment in the glaucophane-rich rim and in some chlorite grains (Figure 8c) provides indirect chemical evidence of the total (or partial) breakdown of one (or more) Mn-rich phase(s) during equilibration of the amphibole rim. Stilpnomelane and carpholite are common Mn-bearing phases in HP–LT rocks (see e.g. Deer et al., 1992). Consequently, it is likely

that the studied calcschist passed through the stilpnomelane- and carpholite-bearing fields at P = 1.6–1.8 GPa, in the presence of phengite with Si p.f.u. = 3.45–3.50, and reached, after stilpnomelane (and/or carpholite) breakdown, the phengite (Si p.f.u. ~ 3.45) + amphibole + paragonite + chlorite + lawsonite + quartz + rutile field, registered by the amphibole rim at P = 1.5–1.6 GPa (Figure 13a). Following this interpretation, the crossite core of amphibole, on the other hand, likely equilibrated on the prograde path or at peak conditions, in the presence of carpholite and/or stilpnomelane. We exclude that the glaucophane rim grew due to the breakdown of lawsonite, as lawsonite usually does not store much Mn (see e.g. Fornash, Whitney, & Seaton, 2019), and lawsonite breakdown is commonly linked to epidote growth (e.g. Evans, 1990). The euhedral epidote grains present in the sample (e.g. Figure 6h) might, in particular, have grown during the retrograde path, following destabilization of lawsonite (Figure 13a, b).

The retrograde assemblage is represented by epidote + plagioclase (albite) + titanite, being stable below 0.6–0.8 GPa. Since all the analyzed phengite equilibrated at peak pressure conditions, it is difficult to constrain the P–T conditions of equilibration of the retrograde assemblage. However, it is likely that the maximum T of retrograde metamorphism were below 400–420 °C, since rutile would have overgrown titanite above these temperatures (Figure 13a, b).

To summarize, we suggest that the peak P–T conditions, reached by the studied calcschist, were P = 1.5–1.8 GPa and T = 320–370 °C (Figure 13a) in the lawsonite-blueschist field, and that the maximum temperatures reached during retrograde metamorphism were around 400–420 °C.

7. Discussion

7.1 Lithostratigraphy and paleogeographic pertinence of the investigated units

The investigated HP–LT metabasic and metacarbonatic rocks belong to a metasedimentary sequence (Acquadolce subunit), which was correlated either with the continental margin of Adria (Barberi et al., 1967b; Keller & Pialli, 1990; Massa et al., 2017) or the oceanic Ligurian Units (Pertusati et al., 1993; Bortolotti et al., 2001). Recently, detrital zircon dating proved that the top of the sequence is early Oligocene in age (Jacobs et al., 2018) and, hence, correlates with the early Apenninic foredeep deposits of the Tuscan margin, as also proposed by Massa et al. (2017). Moreover, according to Bianco et al. (2019), the T/E MORB geochemical affinity of the metabasites excludes any correlation

with the n-MORB ophiolites of the Ligurian Units. However, the early Oligocene minimum deposition age refers to the schistose rocks of the Acquadolce subunit (i.e. sample location in Figure 2). Thus, the age of the calcschist/metabasite lenses entrained in the Acquadolce subunit remains largely unconstrained. Indeed, the only available age constraint is based on the doubtful recognition of Lower Cretaceous microfauna preserved in a limestone layer. Based on this, Massa et al. (2017) correlated the Acquadolce subunit as a whole to the Lower Cretaceous–early Oligocene sequences of the Tuscan margin. However, for a better lithostratigraphic correlation, the following points should be considered:

(1) The metabasites occur as several layers that are interleaved within calcschists and marbles (Figure 3a). The metabasite layers range in thickness between few centimeters and some meters.

(2) The metacarbonate lenses hosting the metabasites display high modal contents of glaucophane, epidote, titanite, chlorite, and albite, with chlorite being more abundant than potassic white mica (Figure 6). Typical blueschist-facies parageneses in metapelitic rocks are characterized by relatively high abundances of K-, Al- and Fe–Mg-bearing phases, such as white mica, chlorite, and chloritoid over Na- and Ca-bearing phases (e.g. Theye, Seidel, & Vidal, 1992; Theye et al., 1997). Indeed, chemical analyses of the studied metapelitic fraction of the calcschist (Table 3) reveal high Ca, Na, Ti, and Mg, and relatively low K content, which is untypical for a standard pelagic shale (see e.g. Carmichael, 1989). Rather, it suggests an input of detrital material from a basic igneous source to the sedimentary protolith of the calcschist.

(3) Detrital allanite (Figure 6e) is present in the calcschists and is modally more abundant than other detrital heavy-minerals, such as zircon. Allanite displays monotonous zoning and euhedral habit (Figure 6e) suggesting that grains of this mineral originated from a fairly restricted igneous source.

Based on the considerations listed above, the Acquadolce metabasites and metacarbonates can be interpreted as associated extrusive magmatic bodies and metavolcanoclastic sequences deposited in a carbonatic sedimentary basin. The source of detrital allanite could be an associated igneous source, which is not outcropping. Detailed investigations of allanite may offer the potential to provide

additional geochemical and geochronological details on the age and characteristics of the volcanic events preserved in the investigated rock record. A similar sequence in the Northern Apennines is found in the Middle Triassic succession of the Punta Bianca and Massa Units (see Figure 1a), where the association of carbonates, alkaline metabasites, and metabreccias was interpreted as evidence of a 'failed' Middle Triassic rift (Martini, Rau, & Tongiorgi, 1986). We therefore suggest that the investigated metabasite was emplaced in the Triassic sequences of the Adria continental margin. The associated marbles and calcschist could be, as a whole, representative of the Triassic–Jurassic passive margin sequences of the Adria margin (e.g. Boccaletti et al., 1971).

The problem that arises from this interpretation is how these – likely Mesozoic – rocks became entrained in the Oligocene foredeep deposits of the Acquadolce subunit. Although new geochronological constraints on the metacarbonatic–metabasic sequences are required, we propose that these carbonate–metabasite lenses were part of an original volcano-sedimentary sequence that was disrupted by tectonic processes during underplating and subsequent exhumation, developing competent lenses surrounded by incompetent schists. Similar examples of entrainment of competent lithologies in a more-deformed matrix are well documented in exhumed blueschist- and eclogite-facies terrains worldwide and have been linked to shearing during subduction (e.g. Kurz, Neubauer, & Dachs, 1998; Angiboust et al., 2011; Kotowski & Behr, 2019).

7.2 P–T constraints from petrographic observations and pseudosection modeling

In the Acquadolce subunit, HP–LT parageneses are well preserved in metabasite and hosting calcschist. Field, petrographic, and pseudosection modelling data document the progressive evolution of the Acquadolce subunit from lawsonite-blueschist to epidote-blueschist and greenschist-facies conditions, in agreement with Bianco et al. (2019). The reconstructed evolution is summarized in Figure 14a. The detailed analysis of metamorphic assemblages and pseudosection modeling in the calcschist constrain the peak P–T conditions of the investigated rocks to 1.5–1.8 GPa and 320–370 °C in the lawsonite-blueschist facies (stage 1 in Figure 14a), based on phengite isopleths. From the pseudosection modelling we infer that lawsonite, paragonite, stilpnomelane, and/or carpholite were likely present as part of the peak metamorphic assemblage in the calcschist (stage 1 in Figure 14a). Lawsonite was not found in the calcschist. However, lawsonite pseudomorphs (Figure 5e; examples

in Tsujimori, Sisson, Liou, Harlow, & Sorensen, 2006; Angiboust, Langdon, Agard, Waters, & Chopin, 2012; López-Carmona et al., 2014) were found in the metabasite (e.g. Figure 5e; stage i–ii in Figure 14a) and also reported by Bianco et al. (2019). Paragonite, which is also predicted to be stable in most blueschist-facies fields above 0.6–1.0 GPa (Figure 10, 11, 13), was not found, as its presence was likely erased by the retrograde growth of albite, both in the metabasite and the calcschist (Figure 5f, 6f). In this sense, it is possible that some of the resorbed pseudomorphs found in albite could have represented former paragonite grains (e.g. Figure 6g).

The strong zoning in Mn of Na-amphibole in the calcschist is likely related to the breakdown of stilpnomelane and/or carpholite close to peak metamorphic conditions (stage 2 in Figure 14a), consistent with a clockwise prograde evolution in the lawsonite-blueschist facies (Figure 14a). Although no precise constraints on the retrograde P–T path are available, the zoning of amphibole from glaucophane–crossite to actinolite (Figure 7a,b; stage i–ii in Figure 14a) and epidote from clinozoisite to Fe-epidote (Figure 7c) in the metabasite, and the blastesis of albite overgrowing Na-amphibole (stage 3 and ii in Figure 14a) indicate retrograde metamorphism along a path from epidote-blueschist to greenschist-facies conditions (e.g. Brown, 1977; Evans, 1990; Davis & Whitney, 2006). Maximum metamorphic temperatures of 380–420 °C can be estimated based on the lack of garnet in both the metabasite and the calcschist (Figure 10a, 13a), thus indicating that the retrograde path was nearly isothermal or characterized by a slight increase in temperature only.

Our P–T estimates are significantly different from those by Bianco et al. (2015), obtained using the jadeite-in-omphacite geobarometer (0.7–0.9 GPa; 330–350 °C). This is because the jadeite-in-omphacite geobarometer provides only minimum pressures. On the other hand, Bianco et al. (2019), were unable to precisely constrain the peak P–T conditions of the Acquadolce metabasite, due to its strong chemical and textural heterogeneities. These authors inferred reasonably $P > 1.6$ GPa and significantly higher temperatures (450–500 °C), based on (1) the former presence of lawsonite and (2) the lack of garnet, which in their modeling, using the Mn-free NCFMASHTO system, appears above 550 °C. However, Mn stabilizes garnet towards low temperature conditions (Spear & Cheney, 1989; Symmes & Ferry, 1992; Mahar et al., 1997; here:380–420 °C). Our modelling of the Acquadolce metabasite (Figure 10) demonstrates, indeed, that such a rock, with strongly zoned amphibole (Figure

7a, b) and clinozoisite-epidote (Figure 7c), is currently of limited use for pseudosection modeling, which requires discernable chemical and textural equilibria.

To summarize, based on the present study, the Acquadolce subunit experienced nearly isothermal exhumation from peak P–T conditions of 1.5–1.8 GPa at 320–370 °C (see P–T path in Figure 14a). Assuming a rock density of 2.8 g/cm^3, the estimated peak pressures indicate maximum depths in the range of 42–50 km. Peak metamorphic conditions were likely attained around 18–20 Ma (^{40}Ar/^{39}Ar white mica age: Deino et al., 1992; ^{40}Ar/^{39}Ar glaucophane age: Bianco et al., 2019). Late Miocene contact metamorphism in the Acquadolce subunit occurred at a maximum pressure of 0.2 GPa (Duranti et al., 1992), corresponding to 5–6 km depth, and was dated at 7–6 Ma (Musumeci et al., 2011, 2015; Viola et al., 2018). Based on the data above, we can estimate an average exhumation rate of 2.5–3.7 km/Ma, which is consistent with those of exhumed blueschist-facies continental units elsewhere (e.g. Ring & Glodny, 2010).

7.3 Implications for early continental collision in the Northern Apennines

In the Northern Tyrrhenian Sea, typical HP–LT ocean-derived units, characterized by metaophiolites and their metasedimentary cover, are found on the Islands of Gorgona and Giglio and in the Argentario promontory (Theye et al., 1997; Rossetti et al., 1999; Orti, Morelli, Pandeli, & Principi, 2002; Elter & Pandeli 2002). Both on Giglio and in the Argentario, HP–LT oceanic units are tectonically stacked over HP–LT carpholite-bearing continental units (Theye et al., 1997). Other HP–LT continental units are found on the mainland, where the HP–LT event is typically recorded by chloritoid- or carpholite-bearing rocks (e.g. Giorgetti et al., 1998; Molli et al., 2000; Lo Pò & Braga, 2014). Based on the present study, the Acquadolce subunit is also a HP–LT continental unit consisting of interleaved metasedimentary and metabasic rocks.

All these units represent scattered remnants of ocean- and continent-derived units that experienced blueschist-facies metamorphism at pressures ranging between 0.7–0.9 GPa and 1.5–1.8 GPa and temperatures between 300 and 420 °C (Figure 14b). The highest pressures are recorded by the oceanic units on the Island of Gorgona (Jolivet et al., 1998) and the continental units on the Island of Elba (this work) (Figure 14b). The coupling of HP–LT oceanic and continental units implies that, during the Oligocene–Early Miocene interval, continental units shared a similar subduction history

with oceanic units in the subduction channel and reached greater depths than previously reported, and attaining metamorphic conditions comparable to those of the subducted oceanic units (i.e. Gorgona island; Jolivet et al., 1998). Based on the available $^{40}Ar/^{39}Ar$ radiometric ages, both continental and oceanic units experienced coeval subduction, exhumation, and tectonic stacking in a short time span (10–15 million years), between 21 and 6 Ma (Figure 14b; Deino et al., 1992; Brunet et al., 2000; Bianco et al., 2019), which implies rapid subduction of continental units and subsequent tectonic coupling with oceanic units during exhumation.

In particular, the estimated P–T values for the Acquadolce subunit are comparable to those reported for some continental units of the western Alps metamorphosed under blueschists- to eclogite-facies conditions, belonging to the Brianzonese zone and the Penninic units. For example, peak P–T conditions of 1.5 GPa at 500 °C have been estimated for glaucophane-bearing micaschist from the Ambin–south Vanoise massif (Ganne, Bussy, & Vidal, 2003), 1.8–2.0 GPa at 490 °C for garnet–chloritoid-bearing micaschists of the Gran Paradiso massif (Chopin, 1981; Le Bayon, Pitra, Ballevre, & Bohn, 2006), and 1.2–1.3 GPa at 425–475 °C for blueschist-facies metasediments of the Combin Unit (Cartwright & Barnicoat, 2002). Significantly lower pressure conditions have been recorded by the continental unit of Alpine Corsica: for instance, the Permian metarhyolites of the Tenda Massif experienced P–T conditions ranging between 0.8 GPa at 300 °C and 1.1 GPa at 500 °C (Tribuzio & Giacomini, 2002) and the Corte slices between 0.8 and 1.4 GPa at 200–350 °C (Di Rosa, Meneghini, Marroni, Hobbs, & Vidal, 2019).

Comparison between HP–LT conditions in the western Alps and in the Tyrrhenian sector of the Northern Apennines suggests that, despite being more recent (Western Alps: 47–33 Ma; Beltrando, Campagnoni, & Lombardo, 2010 and references therein; Northern Apennines: 27–16 Ma; Kligfield et al., 1986; Brunet et al., 2000), the subduction of the Adriatic margin in the Northern Apennines is comparable in depth reached with those of the European margin in the Alps. In both subduction zones, continental crust was involved and experienced P–T conditions related to geothermal gradients of 6–7.5 °C/km. All these features shed new light on the evolution of the hinterland sector of the Northern Apennines, which experienced subduction and exhumation under a very low geothermal gradient, comparable with the 5–10 °C/km reported for oceanic subduction zones (Zheng & Chen, 2016).

7.4 Implications for exhumation processes in the Northern Apennines

In the Northern Apennines metamorphic units are exposed at the base of the nappe stack, at the core of dome-like structures, known as antiformal stacks. The exhumation of these units has been interpreted mostly as the result of (1) post-orogenic extension (Carmignani & Kligfield, 1990; Carmignani et al., 1994) or (2) a combination of syn-orogenic extrusion and post-orogenic extension (Jolivet et al., 1998; Molli et al., 2018).

The present-day setting of the hinterland sector of the Northern Apennines is characterized by extensional seismicity (e.g. Pondrelli et al., 2006), affecting a thinned continental crust (20–25 km at the Tyrrhenian side; Cassinis et al., 2005). This crust is marked by high heat flow, magmatism (e.g. Serri et al., 1993; Della Vedova, Vecellio, Bellani, & Tinivella, 2008), and the presence of wedge-top basins or intermontane basins that have been interpreted as graben fills (see Bonini et al., 2014 for a review). Based on the present-day regime, many authors have suggested long-lasting (post-early Miocene) crustal thinning (e.g. Liotta & Ranalli, 1999; Brogi, Lazzarotto, Liotta, & Ranalli, 2005; Brogi, 2008; Le Breton, Handy, Molli, & Ustaszewski, 2017), favoring a scenario of post-orogenic exhumation in metamorphic core complexes (Carmignani & Kligfield, 1990). In this framework, Bianco et al. (2019) addressed extensional tectonics as the main driver of exhumation of the HP–LT blueschists of the Island of Elba. However, geodetic, geophysical and geodynamic models all suggest that the present geodynamic framework (crustal thickness, seismicity, stress field, and thermal structure of the lithosphere) of the Tyrrhenian sector of Italy can be extrapolated only to the last 2.5 Ma (Faccenna, Becker, Miller, Serpelloni, & Willett, 2014).

On the other hand, several authors (Storti, 1995; Jolivet et al., 1998; Molli et al., 2000; Carosi et al., 2004) noticed that a scenario of pure post-orogenic extension cannot explain (or can only in part explain) many metamorphic and structural features observed in the HP–LT metamorphic units of the Northern Apennines. Jolivet et al. (1998) first suggested that the nearly isothermal exhumation gradient observed in the HP–LT units (e.g. Theye et al., 1997; Giorgetti et al., 1998; Rossetti et al., 1999) indicates syn-orogenic extrusion (examples in Law, Searle, & Godin, 2006; Jolivet & Brun, 2010). Consequently, Jolivet et al. (1998) suggested that this process occurred during the Oligocene–Miocene in the Northern Tyrrhenian Sea before post-orogenic back-arc extension took place. Syn-

orogenic extrusion was also proposed by Molli et al. (2000) and Carosi et al. (2004) to explain the occurrence of higher-grade metamorphic rocks of the Massa Unit (0.6–0.8 GPa at 420–500 °C), sandwiched between the non-metamorphic Tuscan nappe and the Apuane Unit (0.4–0.6 GPa at 360–420 °C) in the Apuan Alps. More recently, Molli et al. (2018) also suggested that the Massa Unit was exhumed in a syn-orogenic setting, due to a combination of deep duplexing and later post-orogenic extension. Both E- and W-verging structures, which have been interpreted as related to syn-orogenic exhumation or gravitational instabilities during underplating of units in the wedge, are preserved in many areas of the Northern Apennines (Storti, 1995; Clemenzi et al., 2014; Massa et al., 2017). Top-to-the-E detachment fault systems, such as the Zuccale Fault on Elba (Collettini & Holdsworth, 2004; Smith, Holdsworth, Collettini, & Pearce, 2011; Musumeci et al., 2015) or the Tellaro Detachment in the La Spezia area (see e.g. Clemenzi et al., 2015) were considered as post-orogenic structures driving the exhumation of metamorphic rocks. However, not only the interpretation of these structures as detachments has been questioned (see Musumeci et al., 2015; Viola et al., 2018), but the total slip measured on these fault systems ranges between 5 to 10 km and thus their contribution for vertical exhumation is minimal (see examples in Ring & Glodny, 2010). High-temperature contact metamorphism (Figure 14b) linked to emplacement of plutons, previously interpreted as post-orogenic magmatism (Jolivet et al., 1998), occurred at very low pressure conditions ($P < 0.2$ GPa; Duranti et al., 1992; Musumeci & Vaselli, 2012; Papeschi et al., 2019) and was coeval with contractional tectonics (e.g. Musumeci et al., 2015; Papeschi et al., 2017; Viola et al., 2018). Moreover, this study highlights that high-temperature metamorphism overprints blueschist-facies rocks that were already exhumed to very shallow levels (Figure 2).

Based on the new metamorphic data from Elba presented here, showing rapid (about 15 Ma) and cold exhumation of blueschist-facies rocks, we, thus, suggest that syn-orogenic extrusion, not post-orogenic extension, was the main process responsible for the exhumation of HP–LT metamorphic units in the hinterland part of the Northern Apennines orogen (Figure 14b). W-verging folds and shear zones, which are documented in many areas of the Northern Apennines (e.g. Gianmarino & Giglia, 1990; Storti, 1995) might have accommodated the extrusion of the deeper units in the orogenic wedge within an overall contractional setting with general E-verging kinematics.

8. Conclusions

This study documents Oligocene–Early Miocene blueschist-facies metamorphism in the Acquadolce subunit from eastern Elba (Northern Apennines, Italy), showing that:

1. The Acquadolce subunit records peak lawsonite-blueschist facies metamorphism at P = 1.5–1.8 GPa and T = 320–370 °C around 21–19 Ma, followed by nearly isothermal exhumation through the epidote-blueschist and albite-greenschist facies at maximum temperatures of 380–420 °C. Peak assemblages were likely characterized by the presence of carpholite and/or stilpnomelane, as suggested by Mn-zoning of glaucophane that likely developed after their breakdown. The 6–7 Ma contact metamorphic overprint occurred at 0.2 GPa, when these rocks where already exhumed, indicating a time frame of at most~15 Ma for exhumation.
2. Metacarbonates contain detrital metabasic material and allanite grains suggesting deposition together with the associated metabasites in a basin that received volcanoclastic input. Lithostratigraphic correlations indicate a possible Triassic age for these rocks, which likely correlate with the metabasite-hosting metacarbonates of the Massa Unit. These rocks might have become enclosed in early Oligocene metapelites due to boudinage or formation of a tectonic mélange in the subduction channel.
3. The underthrusting of the continental Acquadolce subunit to pressures of 1.5–1.8 GPa indicates deep involvement of continental crust in the Apennines in subduction along cold geothermal gradients of 5–10 °C/km. Reached depths are comparable to oceanic units as well as exhumed Europe-derived continental units from the Alps. Retrograde metamorphism along a cold and isothermal gradient supports exhumation by syn-orogenic extrusion, rather than post-orogenic extension.

Acknowledgements

We wish to thank Thomas Theye, Federico Lucci, and Peng-Lei Liu for assistance with the microprobe in Stuttgart. Moritz Schmelz and Massimo Sbrana are warmly thanked for preparing the polished thin section used in this work. Matthias Leiss is thanked for assistance with sample preparation for XRF analysis. Bernardo Cesare and Daria Pascal are acknowledged for wet chemical titration analysis in Padova. We also thank Massimo Pompilio and Alessio di Roberto for assistance

with the SEM in Pisa. This work was supported by the University of Pisa (PRA_2016, Resp. Sergio Rocchi), by the PEGASO PhD program (Tuscany Region, Italy), and by the Erasmus+ exchange program of the European Union. We are in debt to Thomas Lamont and an anonymous reviewer for suggestions to improve the original manuscript. We also thank the editor, Richard White, for his careful editorial work.

References

Andersen, D. J., & Lindsley, D. H. (1988). Internally consistent solution models for Fe-Mg-Mn-Ti oxides; Fe-Ti oxides. *American Mineralogist*, *73*(7-8), 714-726.

Angiboust, S., Agard, P., Raimbourg, H., Yamato, P., & Huet, B. (2011). Subduction interface processes recorded by eclogite-facies shear zones (Monviso, W. Alps). *Lithos*, *127*(1-2), 222-238.

Angiboust, S., Langdon, R., Agard, P., Waters, D., & Chopin, C. (2012). Eclogitization of the Monviso ophiolite (W. Alps) and implications on subduction dynamics. *Journal of Metamorphic Geology*, *30*(1), 37-61.

Aoya, M., Endo, S., Mizukami, T., & Wallis, S. R. (2013). Paleo-mantle wedge preserved in the Sambagawa high-pressure metamorphic belt and the thickness of forearc continental crust. *Geology*, *41*(4), 451-454.

Balestrieri, M. L., Pandeli, E., Bigazzi, G., Carosi, R., & Montomoli, C. (2011). Age and temperature constraints on metamorphism and exhumation of the syn-orogenic metamorphic complexes of Northern Apennines, Italy. *Tectonophysics*, *509*(3-4), 254-271.

Barberi, F., Innocenti, F., & Ricci, C.A. (1967a). Il complesso scistoso di Capo Calamita (Isola d'Elba). *Atti della Società Toscana di Scienze Naturali residente a Pisa, Memorie, Serie A 72 (2),* 579‑617.

Barberi, F., Giglia, G., Innocenti, F., Marinelli, G., Raggi, G., Ricci, C.A., Squarci, P., Taffi, L., & Trevisan, L. (1967b). *Carta geologica dell'isola d'Elba scala 1:25.000*. C.N.R. Roma.

Barboni, M., Annen, C., & Schoene, B. (2015). Evaluating the construction and evolution of upper crustal magma reservoirs with coupled U/Pb zircon geochronology and thermal modeling: A case study from the Mt. Capanne pluton (Elba, Italy). *Earth and Planetary Science Letters*, *432*, 436-448.

Beltrando, M., Compagnoni, R., & Lombardo, B. (2010). (Ultra-) High-pressure metamorphism and orogenesis: an Alpine perspective. *Gondwana Research*, *18*(1), 147-166.

Bernhardt, H. J. (2007). MINCALC-V5, a software tool for mineral analyses data processing. *Acta Microscopica*, *16*(1–2 (Suppl. 2), 43.

Bianco, C., Brogi, A., Caggianelli, A., Giorgetti, G., Liotta, D., & Meccheri, M. (2015). HP-LT metamorphism in Elba Island: implications for the geodynamic evolution of the inner Northern Apennines (Italy). *Journal of Geodynamics*, *91*, 13-25.

Bianco, C., Godard, G., Halton, A., Brogi, A., Liotta, D., & Caggianelli, A. (2019). The lawsonite-glaucophane blueschists of Elba Island (Italy). *Lithos*, *348-349*, 105198.

Biancone, M., & Tucci, P. (1984). The ophiolite rocks of Giglio Island (Tuscan Archipelago). *Ofioliti*, *9*(3), 321-336.

Boccaletti, M., Elter, P., & Guazzone, G. (1971). Plate tectonic models for the development of the Western Alps and Northern Apennines. *Nature Physical Science*, *234*(49), 108-111.

Bonini, M., Sani, F., Stucchi, E. M., Moratti, G., Benvenuti, M., Menanno, G., & Tanini, C. (2014). Late Miocene shortening of the Northern Apennines back-arc. *Journal of Geodynamics*, *74*, 1-31.

Bortolotti, V., Fazzuoli, M., Pandeli, E., Principi, G., Babbini, A., & Corti, S. (2001). Geology of central and eastern Elba Island, Italy. *Ofioliti*, *26*(2a), 97-150.

Bousquet, R., Goffé, B., Vidal, O., Oberhänsli, R., & Patriat, M. (2002). The tectono-metamorphic history of the Valaisan domain from the Western to the Central Alps: New constraints on the evolution of the Alps. *Geological Society of America Bulletin*, *114*(2), 207-225.

Brogi, A. (2008). Kinematics and geometry of Miocene low-angle detachments and exhumation of the metamorphic units in the hinterland of the Northern Apennines (Italy). *Journal of structural Geology*, *30*(1), 2-20.

Brogi, A., & Giorgetti, G. (2012). Tectono-metamorphic evolution of the siliciclastic units in the Middle Tuscan Range (inner Northern Apennines): Mg–carpholite bearing quartz veins related to syn-metamorphic syn-orogenic foliation. *Tectonophysics*, *526*, 167-184.

Brogi, A., Lazzarotto, A., Liotta, D., Ranalli, G., & CROP18 Working Group. (2005). Crustal structures in the geothermal areas of southern Tuscany (Italy): insights from the CROP 18 deep seismic reflection lines. *Journal of Volcanology and Geothermal Research*, *148*(1-2), 60-80.

Brown, E. H. (1977). The crossite content of Ca-amphibole as a guide to pressure of metamorphism. *Journal of Petrology*, *18*(1), 53-72.

Brunet, C., Monié, P., Jolivet, L., & Cadet, J. P. (2000). Migration of compression and extension in the Tyrrhenian Sea, insights from 40Ar/39Ar ages on micas along a transect from Corsica to Tuscany. *Tectonophysics*, *321*(1), 127-155.

Bucher, K., & Grapes, R. (2011). *Petrogenesis of metamorphic rocks*. Springer Science & Business Media.

Bucher-Nurminen, K., Frank, E., & Frey, M. (1983). A model for the progressive regional metamorphism of margarite-bearing rocks in the Central Alps. *American Journal of Science*, *283*(A), 370-395.

Carmichael, R. S. (1989). *Practical Handbook of Physical Properties of Rocks and Minerals*, CRC press, Boca Raton, FL.

Carmignani, L., & Kligfield, R. (1990). Crustal extension in the Northern Apennines: the transition from compression to extension in the Alpi Apuane core complex. *Tectonics*, *9*(6), 1275-1303.

Carmignani, L., Decandia, F. A., Fantozzi, P. L., Lazzarotto, A., Liotta, D., & Meccheri, M. (1994). Tertiary extensional tectonics in Tuscany (northern Apennines, Italy). *Tectonophysics*, *238*(1-4), 295-315.

Caron, J. M. (1994). Metamorphism and deformation in Alpine Corsica. *Schweizerische mineralogische und petrographische mitteilungen*, *74*(1), 105-114.

Carosi, R., Montomoli, C., & Pertusati, P. C. (2004). Late tectonic evolution of the Northern Apennines: the role of contractional tectonics in the exhumation of the Tuscan units. *Geodinamica Acta*, *17*(4), 253-273.

Cartwright, I., & Barnicoat, A. C. (2002). Petrology, geochronology, and tectonics of shear zones in the Zermatt–Saas and Combin zones of the Western Alps. *Journal of Metamorphic Geology*, *20*(2), 263-281.

Cassinis, R., Scarascia, S., Lozej, A., & Finetti, I. R. (2005). Review of seismic wide-angle reflection–refraction (WARR) results in the Italian region (1956–1987). *CROP PROJECT: Deep seismic exploration of the central Mediterranean and Italy*, 31-55.

Chopin, C. (1981). Talc-phengite: a widespread assemblage in high-grade pelitic blueschists of the Western Alps. *Journal of Petrology*, *22*(4), 628-650.

Chopin, C., Beyssac, O., Bernard, S., & Malavieille, J. (2008). Aragonite–grossular intergrowths in eclogite-facies marble, Alpine Corsica. *European Journal of Mineralogy*, *20*(5), 857-865.

Clarke, G. L., Powell, R., & Fitzherbert, J. A. (2006). The lawsonite paradox: a comparison of field evidence and mineral equilibria modelling. *Journal of Metamorphic Geology*, *24*(8), 715-725.

Clemenzi, L., Molli, G., Storti, F., Muchez, P., Swennen, R., & Torelli, L. (2014). Extensional deformation structures within a convergent orogen: the Val di Lima low-angle normal fault system (Northern Apennines, Italy). *Journal of Structural Geology*, *66*, 205-222.

Clemenzi, L., Storti, F., Balsamo, F., Molli, G., Ellam, R., Muchez, P., & Swennen, R. (2015). Fluid pressure cycles, variations in permeability, and weakening mechanisms along low-angle normal faults: The Tellaro detachment, Italy. *Geological Society of America Bulletin*, *127*(11-12), 1689-1710.

Collettini, C., & Holdsworth, R. E. (2004). Fault zone weakening and character of slip along low-angle normal faults: insights from the Zuccale fault, Elba, Italy. *Journal of the Geological Society*, *161*(6), 1039-1051.

Connolly, J. A. (2005). Computation of phase equilibria by linear programming: a tool for geodynamic modeling and its application to subduction zone decarbonation. *Earth and Planetary Science Letters*, *236*(1-2), 524-541.

Connolly, J. A. D. (2009). The geodynamic equation of state: what and how. *Geochemistry, Geophysics, Geosystems*, *10*(10).

Connolly, J. A. D., & Kerrick, D. M. (2002). Metamorphic controls on seismic velocity of subducted oceanic crust at 100–250 km depth. *Earth and Planetary Science Letters*, *204*(1-2), 61-74.

Daniel, J. M., Jolivet, L., Goffé, B., & Poinssot, C. (1996). Crustal-scale strain partitioning: footwall deformation below the Alpine Oligo-Miocene detachment of Corsica. *Journal of Structural Geology*, *18*(1), 41-59.

Davis, P. B., & Whitney, D. L. (2006). Petrogenesis of lawsonite and epidote eclogite and blueschist, Sivrihisar Massif, Turkey. *Journal of Metamorphic Geology*, *24*(9), 823-849.

Della Vedova, B., Vecellio, C., Bellani, S., & Tinivella, U. (2008). Thermal modelling of the Larderello geothermal field (Tuscany, Italy). *International Journal of Earth Sciences*, *97*(2), 317-332.

Deer, W., Howie, R., & Zussman, J. (1992). An introduction to the rock-forming minerals: Essex. *England: Longman Scientific and Technology*.

Deino, A., Keller, J.V.A., Minelli, G., & Pialli, G. (1992). Datazioni $^{40}Ar/^{39}Ar$ del metamorfismo dell'Unità di Ortano-Rio Marina (Isola d'Elba): risultati preliminari. *Studi Geologici Camerti 2*, 187‑192.

Di Rosa, M., Meneghini, F., Marroni, M., Hobbs, N., & Vidal, O. (2019). The Exhumation of Continental Crust in Collisional Belts: Insights from the Deep Structure of Alpine Corsica in the Cima Pedani Area. *The Journal of Geology*, *127*(3), 263-288.

Dini, A., Innocenti, F., Rocchi, S., Tonarini, S., & Westerman, D. S. (2002). The magmatic evolution of the late Miocene laccolith–pluton–dyke granitic complex of Elba Island, Italy. *Geological Magazine*, *139*(3), 257-279.

Durand-Delga, M. (1984). Principaux traits de la Corse alpine et correlations avec les Alpes ligures. *Memorie della Società Geologica Italiana*, *28*, 285-329.

Duranti, S., Palmeri, R., Pertusati, P. C., & Ricci, C. A. (1992). Geological evolution and metamorphic petrology of the basal sequences of eastern Elba (complex II). *Acta Vulcanologica*, *2*, 213-229.

Elter, P., 1975. Introduction a` la géologie de l'Apennin septentrional. *Bull. Soc. Geol. Fr. 7*, 956‑962.

Elter, F. M., & Pandeli, E. (2002). The HP-LP meta-ophiolitic unit and Verrucano of the Cala Grande area in the Argentario Promontory (Southern Tuscany, Italy): structural-metamorphic evolution and regional considerations. *Ofioliti*, *27*(2), 91-102.

Elter, G., Elter, P., Sturani, C., & Weidmann, M., 1966. Sur la prolongation du domaine ligure de l'Apennin less dans le Monferrat et les Alpes et sur l'origine de la Nappe de la Simme e.l. et des Pre´alps romande et chablasiennes. *Archives Science Geneve, 19*, 279–377.

Ernst, W. G. (1973). Blueschist metamorphism and PT regimes in active subduction zones. *Tectonophysics*, *17*(3), 255-272.

Ernst, W. G. (1988). Tectonic history of subduction zones inferred from retrograde blueschist PT paths. *Geology*, *16*(12), 1081-1084.

Ernst, W. G. (2001). Subduction, ultrahigh-pressure metamorphism, and regurgitation of buoyant crustal slices—implications for arcs and continental growth. *Physics of the Earth and Planetary Interiors*, *127*(1-4), 253-275.

Evans, B. W. (1990). Phase relations of epidote-blueschists. Lithos, 25(1-3), 3-23.

Faccenna, C., Becker, T. W., Miller, M. S., Serpelloni, E., & Willett, S. D. (2014). Isostasy, dynamic topography, and the elevation of the Apennines of Italy. *Earth and Planetary Science Letters*, *407*, 163-174.

Fellin, M. G., Reiners, P. W., Brandon, M. T., Wüthrich, E., Balestrieri, M. L., & Molli, G. (2007). Thermochronologic evidence for the exhumational history of the Alpi Apuane metamorphic core complex, northern Apennines, Italy. *Tectonics*, *26*(6).

Fornash, K. F., Whitney, D. L., & Seaton, N. C. (2019). Lawsonite composition and zoning as an archive of metamorphic processes in subduction zones. *Geosphere*, *15*(1), 24-46.

Franceschelli, M., Leoni, L., Memmi, I., & Puxeddu, M. (1986). Regional distribution of Al-silicates and metamorphic zonation in the low-grade Verrucano metasediments from the northern Apennines, Italy. *Journal of Metamorphic Geology*, *4*(3), 309-321.

Fuhrman, M. L., & Lindsley, D. H. (1988). Ternary-feldspar modeling and thermometry. *American mineralogist*, *73*(3-4), 201-215.

Ganne, J., Bussy, F., & Vidal, O. (2003). Multi-stage garnet in the internal Briançonnais basement (Ambin Massif, Savoy): new petrological constraints on the blueschist-facies metamorphism in the Western Alps and tectonic implications. *Journal of Petrology*, *44*(7), 1281-1308.

Gianmarino, S., & Giglia, G. (1990). Gli elementi strutturali della piega di La Spezia nel contesto geodinamico dell'Appennino settentrionale. *Bollettino della Società geologica italiana*, *109*(4), 683-692.

Giorgetti, G., Goffé, B., Memmi, I., & Nieto, F. (1998). Metamorphic evolution of Verrucano metasediments in Northern Apennines; new petrological constraints. *European Journal of Mineralogy*, *10*(6), 1295-1308.

Holland, T. J. B., & Powell, R. (1998). An internally consistent thermodynamic data set for phases of petrological interest. *Journal of metamorphic Geology*, *16*(3), 309-343.

Holland, T. J. B., & Powell, R. (2001). Calculation of phase relations involving haplogranitic melts using an internally consistent thermodynamic dataset. *Journal of Petrology*, *42*(4), 673-683.

Honegger, K., Le Fort, P., Mascle, G., & Zimmermann, J. L. (1989). The blueschists along the Indus suture zone in Ladakh, NW Himalaya. *Journal of Metamorphic Geology*, *7*(1), 57-72.

Jacobs, J., Paoli, G., Rocchi, S., Ksienzyk, A. K., Sirevaag, H., & Elburg, M. A. (2018). Alps to Apennines zircon roller coaster along the Adria microplate margin. *Scientific reports*, *8*(1), 2704.

Jolivet, L., & Brun, J. P. (2010). Cenozoic geodynamic evolution of the Aegean. *International Journal of Earth Sciences, 99*(1), 109-138.

Jolivet, L., Faccenna, C., Goffé, B., Mattei, M., Rossetti, F., Brunet, C., ... & Parra, T. (1998). Midcrustal shear zones in postorogenic extension: example from the northern Tyrrhenian Sea. *Journal of Geophysical Research: Solid Earth*, *103*(B6), 12123-12160.

Keller, J. V. A., & Coward, M. P. (1996). The structure and evolution of the Northern Tyrrhenian Sea. *Geological Magazine, 133*(1), 1-16.

Keller, J.V.A., & Pialli, G. (1990). Tectonics of the island of Elba: a reappraisal. *Bolletino della Società Geologica Italiana, 109*, 413–425.

Kligfield, R., Hunziker, J., Dallmeyer, R. D., & Schamel, S. (1986). Dating of deformation phases using K-Ar and 40Ar/39Ar techniques: results from the Northern Apennines. *Journal of Structural Geology*, *8*(7), 781-798.

Kotowski, A. J., & Behr, W. M. (2019). Length scales and types of heterogeneities along the deep subduction interface: Insights from exhumed rocks on Syros Island, Greece. *Geosphere*, *15*(4), 1038-1065.

Kryza, R., Willner, A. P., Massonne, H. J., Muszyński, A., & Schertl, H. P. (2011). Blueschist-facies metamorphism in the Kaczawa Mountains (Sudetes, SW Poland) of the Central-European Variscides: PT constraints from a jadeite-bearing metatrachyte. *Mineralogical Magazine, 75*(1), 241-263.

Kurz, W., Neubauer, F., & Dachs, E. (1998). Eclogite meso-and microfabrics: implications for the burial and exhumation history of eclogites in the Tauern Window (Eastern Alps) from PTd paths. *Tectonophysics*, *285*(1-2), 183-209.

Law, R. D., Searle, M. P., & Godin, L. (2006). Channel flow, ductile extrusion and exhumation in continental collision zones. Geological Society of London.

Le Bayon, B., Pitra, P., Ballevre, M., & Bohn, M. (2006). Reconstructing P–T paths during continental collision using multi-stage garnet (Gran Paradiso nappe, Western Alps). *Journal of Metamorphic Geology*, *24*(6), 477-496.

Le Breton, E., Handy, M. R., Molli, G., & Ustaszewski, K. (2017). Post-20 Ma motion of the Adriatic Plate: New constraints from surrounding orogens and implications for crust-mantle decoupling. *Tectonics*, *36*(12), 3135-3154.

Liou, J. G., Wang, X., Coleman, R. G., Zhang, Z. M., & Maruyama, S. (1989). Blueschists in major suture zones of China. *Tectonics*, *8*(3), 609-619.

Liotta, D., & Ranalli, G. (1999). Correlation between seismic reflectivity and rheology in extended lithosphere: southern Tuscany, inner Northern Apennines, Italy. *Tectonophysics*, *315*(1-4), 109-122.

Liu, Y., Liu, H., Theye, T., & Massonne, H. J. (2009). Evidence for oceanic subduction at the NE Gondwana margin during Permo-Triassic times. *Terra Nova*, *21*(3), 195-202.

Lo Pò, D., & Braga, R. (2014). Influence of ferric iron on phase equilibria in greenschist facies assemblages: the hematite-rich metasedimentary rocks from the Monti Pisani (Northern Apennines). *Journal of Metamorphic Geology*, *32*(4), 371-387.

López-Carmona, A., Pitra, P., & Abati, J. (2013). Blueschist-facies metapelites from the Malpica–Tui Unit (NW Iberian Massif): phase equilibria modelling and H2O and Fe2O3 influence in high-pressure assemblages. *Journal of Metamorphic Geology*, *31*(3), 263-280.

López-Carmona, A., Abati, J., Pitra, P., & Lee, J. K. (2014). Retrogressed lawsonite blueschists from the NW Iberian Massif: P–T–t constraints from thermodynamic modelling and 40 Ar/39 Ar geochronology. *Contributions to Mineralogy and Petrology*, *167*(3), 987.

Mahar, E. M., Baker, J. M., Powell, R., Holland, T. J. B., & Howell, N. (1997). The effect of Mn on mineral stability in metapelites. *Journal of Metamorphic Geology*, *15*(2), 223-238.

Maineri, C., Benvenuti, M., Costagliola, P., Dini, A., Lattanzi, P., Ruggieri, G., & Villa, I. M. (2003). Sericitic alteration at the La Crocetta deposit (Elba Island, Italy): interplay between magmatism, tectonics and hydrothermal activity. *Mineralium Deposita*, *38*(1), 67-86.

Malavieille, J., Chemenda, A., & Larroque, C. (1998). Evolutionary model for Alpine Corsica: mechanism for ophiolite emplacement and exhumation of high-pressure rocks. *Terra Nova*, *10*, 317-322.

Malinverno, A., & Ryan, W. B. (1986). Extension in the Tyrrhenian Sea and shortening in the Apennines as result of arc migration driven by sinking of the lithosphere. *Tectonics*, *5*(2), 227-245.

Martini, I. P., Rau, A., & Tongiorgi, M. (1986). Syntectonic sedimentation in a Middle Triassic rift, northern Apennines, Italy. *Sedimentary Geology*, *47*(3-4), 191-219.

Maruyama, S., Liou, J. G., & Terabayashi, M. (1996). Blueschists and eclogites of the world and their exhumation. *International geology review*, *38*(6), 485-594.

Massa, G., Musumeci, G., Mazzarini, F., & Pieruccioni, D. (2017). Coexistence of contractional and extensional tectonics during the northern Apennines orogeny: the late Miocene out-of-sequence thrust in the Elba Island nappe stack. *Geological Journal*, *52*(3), 353-368.

Massonne, H. J. (2010). Phase relations and dehydration behaviour of calcareous sediments at very-low to low grade metamorphic conditions. *Periodico di Mineralogia*, *79*(2), 21-43.

Massonne, H. J., & Schreyer, W. (1986). High-pressure syntheses and X-ray properties of white micas in the system K2O-MgO-Al2O3-SiO2-H2O. *Neues Jahrbuch für Mineralogie. Abhandlungen*, *153*(2), 177-215.

Massonne, H. J., & Willner, A. P. (2008). Phase relations and dehydration behaviour of psammopelite and mid-ocean ridge basalt at very-low-grade to low-grade metamorphic conditions. *European Journal of Mineralogy*, *20*(5), 867-879.

Miyashiro, A. (1961). Evolution of metamorphic belts. *Journal of petrology*, *2*(3), 277-311.

Molli, G. (2008). Northern Apennine–Corsica orogenic system: an updated overview. *Geological Society, London, Special Publications*, *298*(1), 413-442.

Molli, G., Giorgetti, G., & Meccheri, M. (2000). Structural and petrological constraints on the tectono-metamorphic evolution of the Massa Unit (Alpi Apuane, NW Tuscany, Italy). *Geological Journal*, *35*(3-4), 251-264.

Molli, G., Vitale Brovarone, A., Beyssac, O., & Cinquini, I. (2018). RSCM thermometry in the Alpi Apuane (NW Tuscany, Italy): New constraints for the metamorphic and tectonic history of the inner northern Apennines. *Journal of Structural Geology*, *113*, 200-216.

Musumeci, G., & Vaselli, L. (2012). Neogene deformation and granite emplacement in the metamorphic units of northern Apennines (Italy): Insights from mylonitic marbles in the Porto Azzurro pluton contact aureole (Elba Island). *Geosphere*, *8*(2), 470-490.

Musumeci, G., Mazzarini, F., Tiepolo, M., & Di Vincenzo, G. (2011). U-Pb and 40Ar-39Ar geochronology of Palaeozoic units in the northern Apennines: determining protolith age and alpine evolution using the Calamita Schist and Ortano Porphyroid. *Geological Journal*, *46*(4), 288-310.

Musumeci, G., Mazzarini, F., & Cruden, A. R. (2015). The Zuccale Fault, Elba Island, Italy: a new perspective from fault architecture. *Tectonics*, *34*(6), 1195-1218.

Orti, L., Morelli, M., Pandeli, E., & Principi, G. (2002). New geological data from Gorgona Island (Northern Tyrrhenian Sea). *Ofioliti*, *27*(2), 133-144.

Papeschi, S., Musumeci, G., & Mazzarini, F. (2017). Heterogeneous brittle-ductile deformation at shallow crustal levels under high thermal conditions: The case of a synkinematic contact aureole in the inner northern Apennines, southeastern Elba Island, Italy. *Tectonophysics*, *717*, 547-564.

Papeschi, S., Musumeci, G., Massonne, H.J., Bartoli, O., & Cesare, B. (2019). Partial melting and strain localization in metapelites at very low-pressure conditions: the northern Apennines magmatic arc on the Island of Elba, Italy. *Lithos*, 105230.

Pertusati, P. C., Raggi, G., Ricci, C. A., Duranti, S., & Palmeri, R. (1993). Evoluzione post-collisionale dell'Elba centro-orientale. *Memorie della Società Geologica Italiana*, *49*, 297-312.

Platt, J. P. (1993). Exhumation of high-pressure rocks: A review of concepts and processes. *Terra nova*, *5*(2), 119-133.

Pondrelli, S., Salimbeni, S., Ekström, G., Morelli, A., Gasperini, P., & Vannucci, G. (2006). The Italian CMT dataset from 1977 to the present. *Physics of the Earth and Planetary Interiors*, *159*(3-4), 286-303.

Powell, R., & Holland, T. J. B. (1999). Relating formulations of the thermodynamics of mineral solid solutions; activity modeling of pyroxenes, amphiboles, and micas. *American Mineralogist*, *84*(1-2), 1-14.

Ring, U., & Layer, P. W. (2003). High-pressure metamorphism in the Aegean, eastern Mediterranean: Underplating and exhumation from the Late Cretaceous until the Miocene to Recent above the retreating Hellenic subduction zone. *Tectonics*, *22*(3).

Ring, U., & Glodny, J. (2010). No need for lithospheric extension for exhuming (U) HP rocks by normal faulting. *Journal of the Geological Society*, *167*(2), 225-228.

Ring, U., Brandon, M. T., Willett, S. D., & Lister, G. S. (1999). Exhumation processes. *Geological Society, London, Special Publications*, *154*(1), 1-27.

Rossetti, F., Faccenna, C., Jolivet, L., Funiciello, R., Tecce, F., & Brunet, C. (1999). Syn-versus post-orogenic extension: the case study of Giglio Island (Northern Tyrrhenian Sea, Italy). *Tectonophysics*, *304*(1-2), 71-93.

Rossetti, F., Faccenna, C., Jolivet, L., Goffé, B., & Funiciello, R. (2002). Structural signature and exhumation P-T-t paths of the blueschist units exposed in the interior of the Northern Apennine chain, tectonic implications. *Bollettino della Società geologica italiana*, *121*(1), 829-842.

Rossetti, F., Glodny, J., Theye, T., & Maggi, M. (2015). Pressure–temperature–deformation–time of the ductile Alpine shearing in Corsica: From orogenic construction to collapse. *Lithos*, *218*, 99-116.

Searle, M. P., & Lamont, T. N. (2020). Compressional metamorphic core complexes, low-angle normal faults and extensional fabrics in compressional tectonic settings. *Geological Magazine*, *157*(1), 101-118.

Serri, G., Innocenti, F., & Manetti, P. (1993). Geochemical and petrological evidence of the subduction of delaminated Adriatic continental lithosphere in the genesis of the Neogene-Quaternary magmatism of central Italy. *Tectonophysics*, *223*(1-2), 117-147.

Siivola, J., & Schmid, R. (2007). List of mineral abbreviations. *Metamorphic Rocks: A Classification and Glossary of Terms. Recommendations of the International Union of Geological Sciences Subcommission on the Systematics of Metamorphic Rocks*, 93-110.

Smith, S. A. F., Holdsworth, R. E., Collettini, C., & Pearce, M. A. (2011). The microstructural character and mechanical significance of fault rocks associated with a continental low-angle normal fault: the Zuccale Fault, Elba Island, Italy. *Geological Society, London, Special Publications*, *359*(1), 97-113.

Spear, F. S., & Cheney, J. T. (1989). A petrogenetic grid for pelitic schists in the system SiO_2-Al$_2O_3$-FeO-MgO-K_2O-H_2O. *Contributions to Mineralogy and Petrology*, *101*(2), 149-164.

Stern, R. J. (2005). Evidence from ophiolites, blueschists, and ultrahigh-pressure metamorphic terranes that the modern episode of subduction tectonics began in Neoproterozoic time. *Geology*, *33*(7), 557-560.

Storti, F. (1995). Tectonics of the Punta Bianca promontory: Insights for the evolution of the Northern Apennines-Northern Tyrrhenian Sea basin. *Tectonics*, *14*(4), 832-847.

Symmes, G. H., & Ferry, J. M. (1992). The effect of whole-rock MnO content on the stability of garnet in pelitic schists during metamorphism. *Journal of Metamorphic Geology*, *10*(2), 221-237.

Tajčmanová, L., Connolly, J. A. D., & Cesare, B. (2009). A thermodynamic model for titanium and ferric iron solution in biotite. *Journal of Metamorphic Geology*, *27*(2), 153-165.

Theye, T., Seidel, E., & Vidal, O. (1992). Carpholite, sudoite, and chloritoid in low-grade high-pressure metapelites from Crete and the Peloponnese, Greece. *European Journal of Mineralogy*, 487-508.

Theye, T., Reinhardt, J., Goffé, B., Jolivet, L., & Brunet, C. (1997). Ferro-and magnesiocarpholite from the Monte Argentario (Italy): First evidence for high-pressure metamorphism of the metasedimentary Verrucano sequence, and significance for PT path reconstruction. *European Journal of Mineralogy*, 859-874.

Tindle, A. G., & Webb, P. C. (1994). PROBE-AMPH—a spreadsheet program to classify microprobe-derived amphibole analyses. *Computers & Geosciences*, *20*(7-8), 1201-1228.

Tribuzio, R., & Giacomini, F. (2002). Blueschist facies metamorphism of peralkaline rhyolites from the Tenda crystalline massif (northern Corsica): evidence for involvement in the Alpine subduction event?. *Journal of Metamorphic Geology*, *20*(5), 513-526.

Tsujimori, T., & Ernst, W. G. (2014). Lawsonite blueschists and lawsonite eclogites as proxies for palaeo-subduction zone processes: a review. *Journal of Metamorphic Geology*, *32*(5), 437-454.

Tsujimori, T., Sisson, V. B., Liou, J. G., Harlow, G. E., & Sorensen, S. S. (2006). Very-low-temperature record of the subduction process: A review of worldwide lawsonite eclogites. *Lithos*, *92*(3-4), 609-624.

Vitale Brovarone, A., & Herwartz, D. (2013). Timing of HP metamorphism in the Schistes Lustrés of Alpine Corsica: New Lu–Hf garnet and lawsonite ages. *Lithos*, *172*, 175-191.

Vitale Brovarone, A., Groppo, C., Hetényi, G., Compagnoni, R., & Malavieille, J. (2011). Coexistence of lawsonite-bearing eclogite and blueschist: phase equilibria modelling of Alpine Corsica metabasalts and petrological evolution of subducting slabs. *Journal of Metamorphic Geology*, *29*(5), 583-600.

Vitale Brovarone, A., Beyssac, O., Malavieille, J., Molli, G., Beltrando, M., & Compagnoni, R. (2013). Stacking and metamorphism of continuous segments of subducted lithosphere in a high-pressure wedge: the example of Alpine Corsica (France). *Earth-Science Reviews*, *116*, 35-56.

Viola, G., Torgersen, E., Mazzarini, F., Musumeci, G., van der Lelij, R., Schönenberger, J., & Garofalo, P. S. (2018). New Constraints on the Evolution of the Inner Northern Apennines by K-Ar Dating of Late Miocene-Early Pliocene Compression on the Island of Elba, Italy. *Tectonics*, *37*(9), 3229-3243.

Warren, C. J., & Waters, D. J. (2006). Oxidized eclogites and garnet-blueschists from Oman: P–T path modelling in the NCFMASHO system. *Journal of Metamorphic Geology*, *24*(9), 783-802.

Zheng, Y. F., & Chen, Y. X. (2016). Continental versus oceanic subduction zones. *National Science Review*, *3*(4), 495-519.

Supporting Information

Additional supporting information may be found online in the Supporting Information section at the end of the article. The microprobe source files (settings, core files and exported images), XRF analysis and phase equilibria modeling files related to this manuscript are available at Papeschi, Samuele; Massonne, Hans-Joachim; Musumeci, Giovanni (2019), "Microprobe data and pseudosection files - Samples IESP3SP53 & IESP3SP56 - Acquadolce subunit - Elba (Italy)", Mendeley Data, v1 http://dx.doi.org/10.17632/x73vj9572h.1

Table S1 – List of the investigated samples, as they appear on SESAR (https://app.geosamples.org/). Minerals in assemblage and accessories are in modal order from high to low. The classification follows the IUGS recommendations for the nomenclature of metamorphic rocks. Abbreviations after Siivola & Schmid (2007).

Section S1– Spot and area location - Sample IESP3SP56

Section S2 – Spot and area location - Sample IESP3SP53

Section S3 – Mineral chemistry – Sample IESP3SP56

Section S4 – Mineral chemistry – Sample IESP3SP53

Section S5 – Phase equilibria modeling

Table 1 – Representative mineral analyses in the metabasite sample (IESP3SP56).

	Epidote				Amphibole					Chlorite		Albite		Titanite	
	core		rim		core		rim		matrix						
Analysis	17	20	14	72	2	33	28	87	96	5	90	32	97	27	62
SiO_2	42.80	39.02	37.61	37.54	56.45	58.83	56.36	55.62	54.15	28.40	29.68	68.96	68.34	31.81	30.23
TiO_2	0.16	0.31	0.05	0.07	0.14	0.06	0.01	0.00	0.04	0.00	0.00	0.02	0.00	37.03	39.25
Al_2O_3	34.62	31.17	24.76	22.28	7.88	11.01	0.80	1.10	2.37	18.93	19.37	19.06	18.86	1.58	0.69
FeOtot	0.49	2.69	9.97	12.98	15.35	10.45	10.28	10.01	12.39	18.78	15.74	0.41	0.27	0.60	0.57
MnO	0.00	0.07	0.08	0.06	0.11	0.12	0.17	0.26	0.19	0.35	0.34	0.03	0.00	0.04	0.01
MgO	0.02	0.06	0.23	0.01	9.79	10.16	17.53	17.72	15.90	21.56	21.27	0.02	0.02	0.03	0.05
CaO	19.85	24.48	23.01	23.12	0.72	0.41	12.25	11.54	11.45	0.19	0.19	0.15	0.11	27.68	28.32
BaO	0.00	0.02	0.00	0.00	0.00	0.00	0.02	0.00	0.01	0.04	0.00	0.01	0.02	1.21	1.25
Na_2O	0.28	0.00	0.01	0.01	0.06	0.01	0.03	0.05	0.10	0.06	0.03	11.98	12.16	0.16	0.08
K_2O	0.02	0.00	0.00	0.00	6.22	7.06	0.43	0.84	0.87	0.03	0.03	0.05	0.05	0.02	0.02
Total	98.24	97.82	95.72	96.08	96.71	98.09	97.88	97.14	97.46	88.35	86.63	100.7	99.83	100.2	100.5
Si	3.16	2.99	3.00	3.01	7.86	7.98	7.95	7.87	7.72	2.87	2.99	3.00	3.00	1.04	0.99
Al	3.01	2.81	2.33	2.11	1.29	1.76	0.13	0.18	0.40	2.25	2.30	0.98	0.98	0.06	0.03
Ti	0.01	0.02	0.00	0.00	0.01	0.01	0.00	0.00	0.00	0.00	0.00	0.00	0.00	0.91	0.97
Fe^{2+}	0.00	0.00	0.00	0.00	0.74	0.89	1.07	0.84	1.08	1.59	1.33	0.00	0.00	0.02	0.02
Fe^{3+}	0.03	0.17	0.67	0.87	1.05	0.29	0.14	0.35	0.40	0.00	0.00	0.01	0.01	0.00	0.00
Mn	0.00	0.00	0.01	0.00	0.01	0.01	0.02	0.03	0.02	0.03	0.03	0.00	0.00	0.00	0.00
Mg	0.00	0.01	0.03	0.00	2.03	2.05	3.69	3.73	3.38	3.24	3.19	0.00	0.00	0.00	0.00
Ca	1.57	2.01	1.97	1.99	0.11	0.06	1.85	1.75	1.75	0.02	0.02	0.01	0.01	0.97	1.00
Ba	0.00	0.00	0.00	0.00	0.00	0.00	0.00	0.00	0.00	0.00	0.00	0.00	0.00	0.02	0.02
Na	0.04	0.00	0.00	0.00	1.68	1.86	0.12	0.23	0.24	0.01	0.01	1.01	1.03	0.01	0.00
K	0.00	0.00	0.00	0.00	0.01	0.00	0.01	0.01	0.02	0.00	0.00	0.00	0.00	0.00	0.00

Table 2 – Representative mineral analyses in the calcschist sample (IESP3SP53). Mineral abbreviations after Siivola & Schmid (2007)

	Amphibole				Phengite					Chlorite		Epidote		Ab	Ttn
	core		rim												
Analysis	149	150	152	154	20	75	78	117	127	32	94	12	54	157	104
SiO_2	56.76	57.17	58.17	58.03	52.44	51.77	51.74	52.02	52.50	28.51	28.04	37.63	37.96	68.85	30.78
TiO_2	0.21	0.12	0.09	0.09	0.06	0.06	0.08	0.01	0.07	0.02	0.02	0.01	0.08	0.01	38.59
Al_2O_3	5.47	5.74	10.25	9.03	24.55	25.29	24.72	25.07	24.38	18.41	19.21	22.03	21.59	19.49	0.95
Cr_2O_3	0.00	0.00	0.00	0.00	0.00	0.00	0.00	0.00	0.00	0.00	0.00	0.00	0.00	0.00	0.00
FeOtot	16.86	16.26	10.38	11.26	2.93	3.23	3.77	2.43	3.28	17.29	18.05	13.83	14.68	0.06	0.51
MnO	0.10	0.11	0.39	0.51	0.10	0.11	0.05	0.11	0.12	0.61	0.93	0.01	0.28	0.00	0.08
MgO	10.64	10.24	11.02	10.92	4.32	4.16	4.12	4.43	4.45	22.71	21.30	0.00	0.02	0.00	0.00
CaO	0.27	0.15	0.26	0.41	0.08	0.04	0.01	0.15	0.08	0.07	0.01	23.14	23.40	0.11	28.14
BaO	0.01	0.00	0.00	0.00	0.12	0.09	0.11	0.12	0.13	0.01	0.00	0.00	0.10	0.00	1.32
Na_2O	6.98	6.82	7.41	7.27	0.15	0.10	0.06	0.10	0.08	0.01	0.01	0.02	0.00	11.92	0.06
K_2O	0.01	0.02	0.00	0.00	10.79	11.24	11.18	11.67	10.94	0.09	0.03	0.00	0.01	0.03	0.07
Total	97.31	96.63	97.97	97.52	95.56	96.09	95.84	96.11	96.01	87.72	87.61	96.67	98.14	100.5	100.5
Si	7.90	7.99	7.90	7.95	3.51	3.46	3.47	3.47	3.50	2.88	2.85	3.01	3.00	3.00	1.01
Al	0.90	0.95	1.64	1.46	1.93	1.99	1.95	1.97	1.92	2.19	2.30	2.08	2.01	1.00	0.04
Ti	0.02	0.01	0.01	0.01	0.00	0.00	0.00	0.00	0.00	0.00	0.00	0.00	0.00	0.00	0.95
Cr	0.00	0.00	0.00	0.00	0.00	0.00	0.00	0.00	0.00	0.00	0.00	0.00	0.00	0.00	0.00
Fe^{2+}	0.67	0.76	0.66	0.72	0.16	0.18	0.21	0.14	0.18	1.46	1.53	0.00	0.00	0.00	0.01
Fe^{3+}	1.29	1.15	0.52	0.57	0.00	0.00	0.00	0.00	0.00	0.00	0.00	0.92	0.97	0.00	0.00
Mn	0.01	0.01	0.05	0.06	0.01	0.01	0.00	0.01	0.01	0.05	0.08	0.00	0.02	0.00	0.00
Mg	2.21	2.13	2.23	2.23	0.43	0.41	0.41	0.44	0.44	3.42	3.23	0.00	0.00	0.00	0.00
Ca	0.04	0.02	0.04	0.06	0.01	0.00	0.00	0.01	0.01	0.01	0.00	1.98	1.98	0.01	0.99
Ba	0.00	0.00	0.00	0.00	0.00	0.00	0.00	0.00	0.00	0.00	0.00	0.00	0.00	0.00	0.02
Na	1.88	1.85	1.95	1.93	0.02	0.01	0.01	0.01	0.01	0.00	0.00	0.00	0.00	1.01	0.00
K	0.00	0.00	0.00	0.00	0.92	0.96	0.96	0.99	0.93	0.01	0.00	0.00	0.00	0.00	0.00

Table 3 – Bulk-rock composition from XRF analyses and wet chemical titration of the investigated samples (left columns), recalculated from the MnNCKFMASHTO system (right columns), expressed in wt%.

Analysis			MnNCKFMASHTO		
	Metabasite (IESP3SP56)	Calcschist (IESP3SP53)		Metabasite (IESP3SP56)	Calcschist (IESP3SP53)
SiO_2	48.55	53.30	SiO_2	50.89	55.99
TiO_2	1.15	0.90	TiO_2	1.21	0.94
Al_2O_3	18.28	16.52	Al_2O_3	19.16	17.36
FeO	4.04	4.01	FeO	7.79	8.28
Fe_2O_3	3.78	4.76	O_2	0.39	0.45
MnO	0.13	0.21	MnO	0.13	0.22
MgO	8.34	9.15	MgO	8.74	9.61
CaO	8.26	2.34	CaO	8.47	2.46
Na_2O	2.73	2.62	Na_2O	2.86	2.76
K_2O	0.32	1.84	K_2O	0.33	1.94
P_2O5	0.13	0	P_2O5	-	-

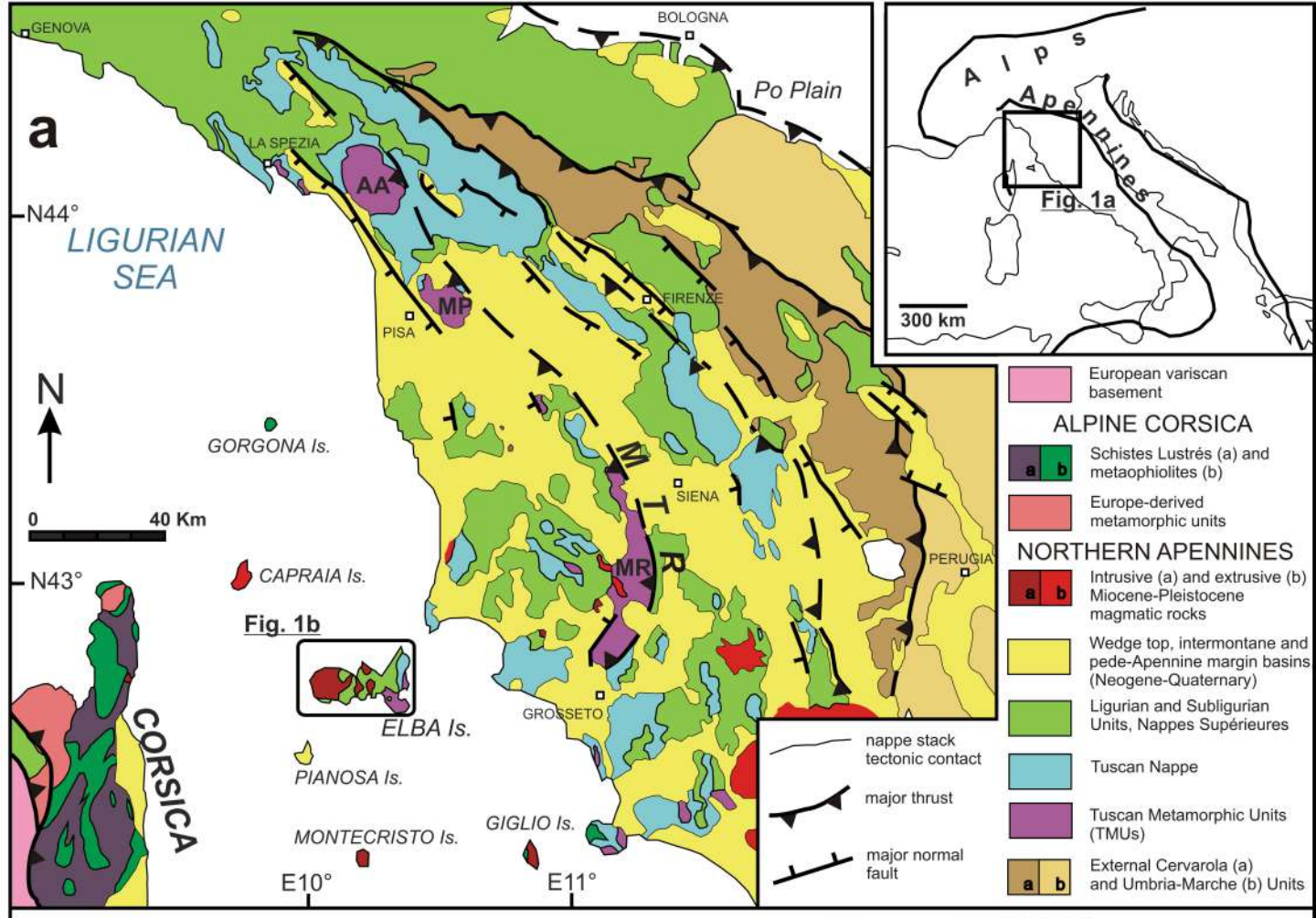
a
GENOVA
BOLOGNA
Po Plain
LA SPEZIA
AA
N44°
LIGURIAN SEA
MP
PISA
FIRENZE
N
GORGONA Is.
0 40 Km
MT
MR
SIENA
PERUGIA
N43°
CAPRAIA Is.
Fig. 1b
ELBA Is.
CORSICA
GROSSETO
PIANOSA Is.
MONTECRISTO Is.
GIGLIO Is.
E10°
E11°
Alps
Apennines
Fig. 1a
300 km
European variscan basement
ALPINE CORSICA
Schistes Lustrés (a) and metaophiolites (b)
Europe-derived metamorphic units
NORTHERN APENNINES
Intrusive (a) and extrusive (b) Miocene-Pleistocene magmatic rocks
Wedge top, intermontane and pede-Apennine margin basins (Neogene-Quaternary)
Ligurian and Subligurian Units, Nappes Supérieures
Tuscan Nappe
Tuscan Metamorphic Units (TMUs)
External Cervarola (a) and Umbria-Marche (b) Units
nappe stack tectonic contact
major thrust
major normal fault

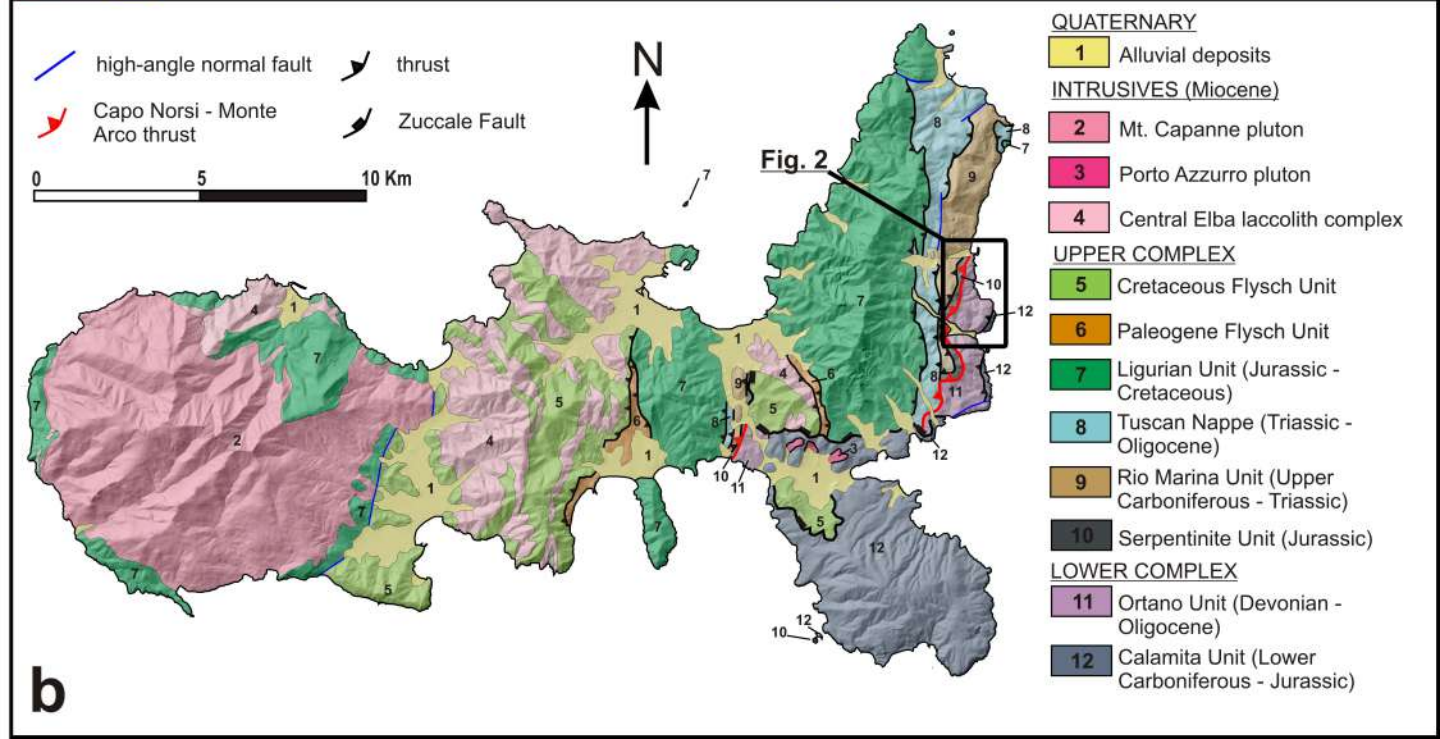
high-angle normal fault
thrust
Capo Norsi - Monte Arco thrust
Zuccale Fault
N
0 5 10 Km
Fig. 2
b
QUATERNARY
1 Alluvial deposits
INTRUSIVES (Miocene)
2 Mt. Capanne pluton
3 Porto Azzurro pluton
4 Central Elba laccolith complex
UPPER COMPLEX
5 Cretaceous Flysch Unit
6 Paleogene Flysch Unit
7 Ligurian Unit (Jurassic - Cretaceous)
8 Tuscan Nappe (Triassic - Oligocene)
9 Rio Marina Unit (Upper Carboniferous - Triassic)
10 Serpentinite Unit (Jurassic)
LOWER COMPLEX
11 Ortano Unit (Devonian - Oligocene)
12 Calamita Unit (Lower Carboniferous - Jurassic)

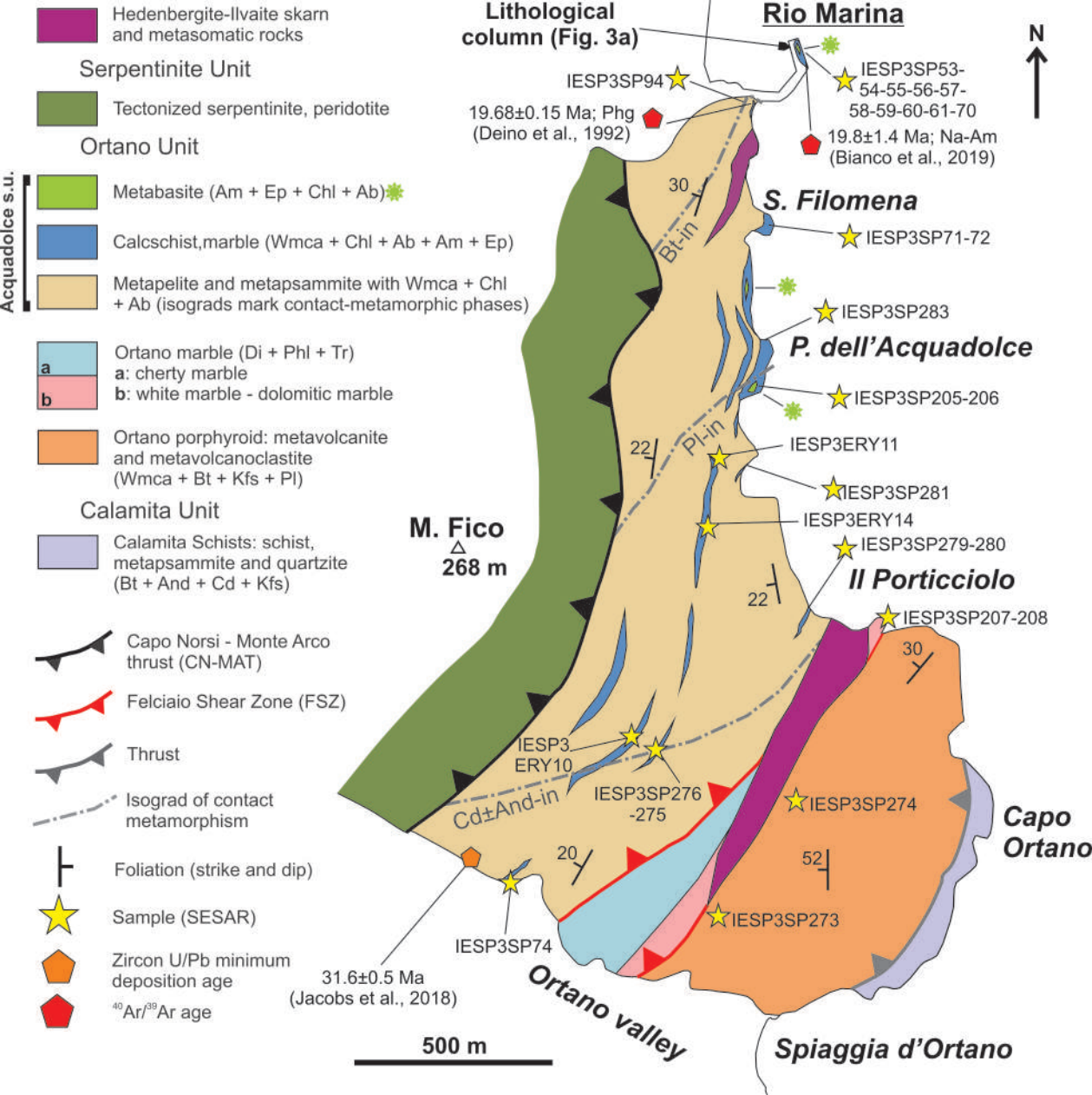
Hedenbergite-Ilvaite skarn and metasomatic rocks
Serpentinite Unit
Tectonized serpentinite, peridotite
Ortano Unit
Acquadolce s.u.
Metabasite (Am + Ep + Chl + Ab)
Calcschist,marble (Wmca + Chl + Ab + Am + Ep)
Metapelite and metapsammite with Wmca + Chl + Ab (isograds mark contact-metamorphic phases)
a
b
Ortano marble (Di + Phl + Tr)
a: cherty marble
b: white marble - dolomitic marble
Ortano porphyroid: metavolcanite and metavolcanoclastite (Wmca + Bt + Kfs + Pl)
Calamita Unit
Calamita Schists: schist, metapsammite and quartzite (Bt + And + Cd + Kfs)
Capo Norsi - Monte Arco thrust (CN-MAT)
Felciaio Shear Zone (FSZ)
Thrust
Isograd of contact metamorphism
Foliation (strike and dip)
Sample (SESAR)
Zircon U/Pb minimum deposition age
40Ar/39Ar age
Lithological column (Fig. 3a)
Rio Marina
N
IESP3SP94
IESP3SP53-54-55-56-57-58-59-60-61-70
19.68±0.15 Ma; Phg (Deino et al., 1992)
19.8±1.4 Ma; Na-Am (Bianco et al., 2019)
30
Bt-in
S. Filomena
IESP3SP71-72
IESP3SP283
P. dell'Acquadolce
IESP3SP205-206
22
Pl-in
IESP3ERY11
IESP3SP281
IESP3ERY14
IESP3SP279-280
M. Fico
268 m
22
Il Porticciolo
IESP3SP207-208
30
IESP3ERY10
IESP3SP276-275
Cd±And-in
IESP3SP274
Capo Ortano
20
52
IESP3SP273
IESP3SP74
31.6±0.5 Ma (Jacobs et al., 2018)
Ortano valley
Spiaggia d'Ortano
500 m

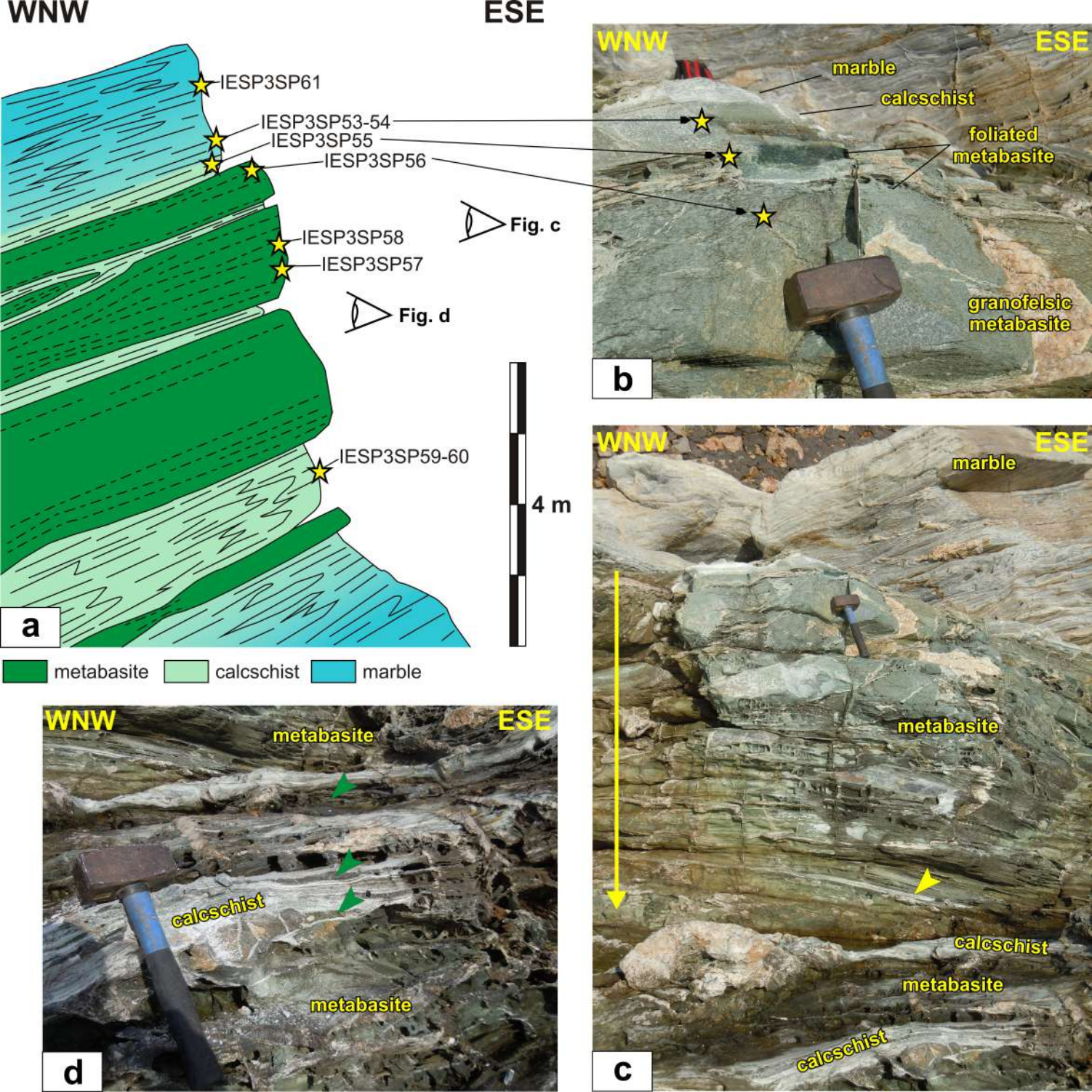
WNW
ESE
IESP3SP61
IESP3SP53-54
IESP3SP55
IESP3SP56
Fig. c
IESP3SP58
IESP3SP57
Fig. d
IESP3SP59-60
4 m
a
metabasite
calcschist
marble
WNW
ESE
marble
calcschist
foliated metabasite
granofelsic metabasite
b
WNW
ESE
marble
metabasite
calcschist
metabasite
calcschist
c
WNW
ESE
metabasite
calcschist
metabasite
d

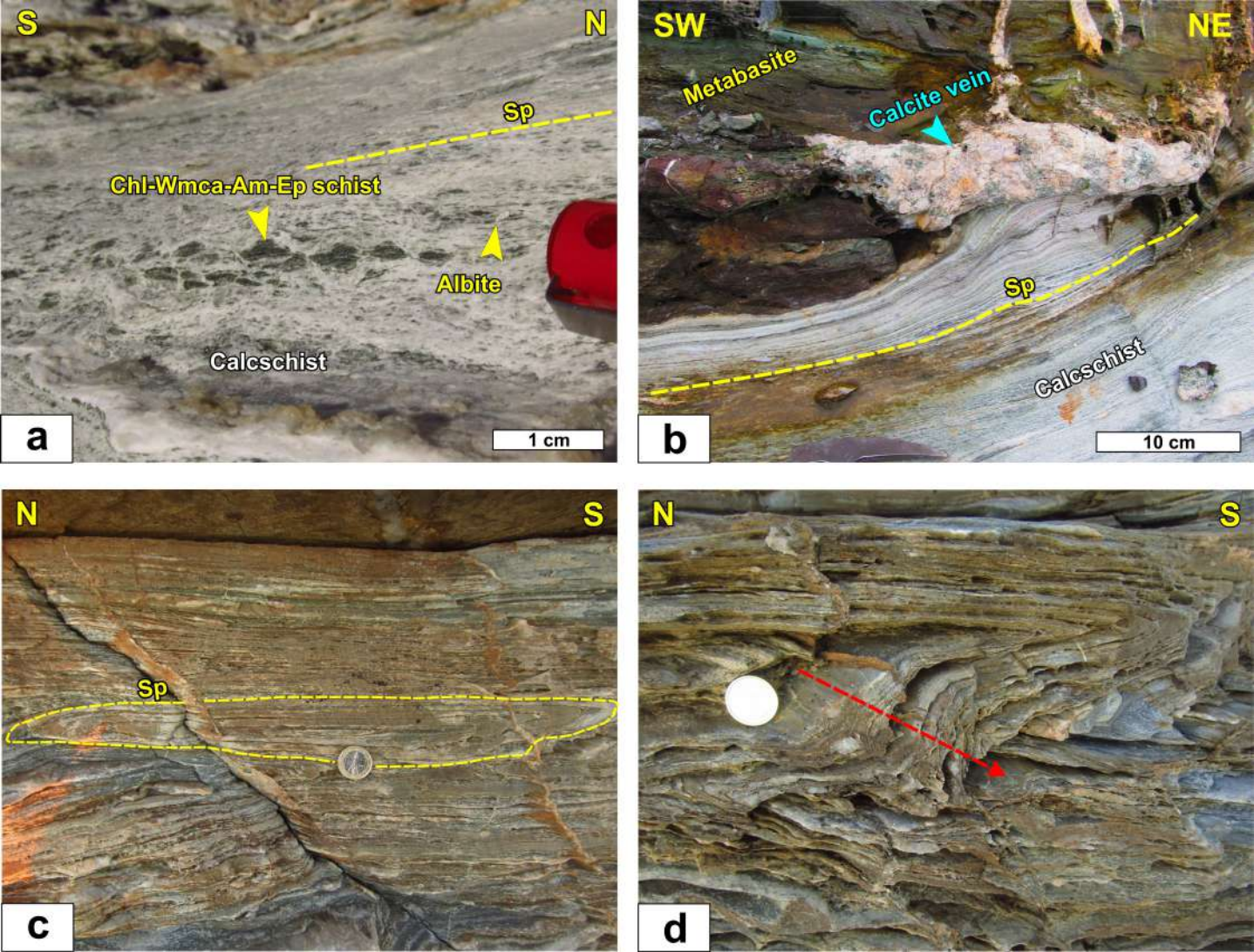
S
N
Sp
Chl-Wmca-Am-Ep schist
Albite
Calcschist
a
1 cm
SW
NE
Metabasite
Calcite vein
Sp
Calcschist
b
10 cm
N
S
Sp
c
N
S
d

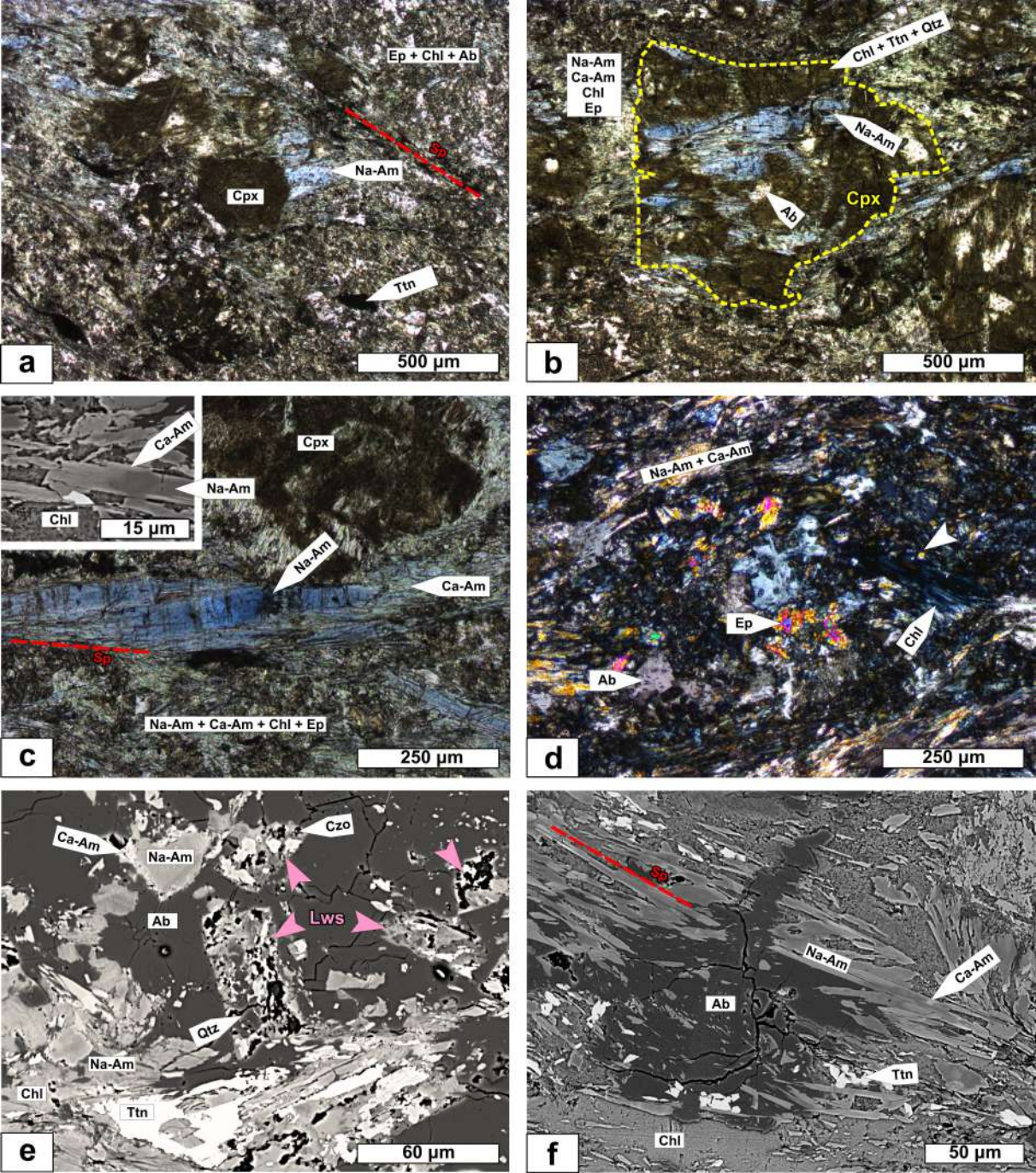
Ep + Chl + Ab
Sp
Na-Am
Cpx
Ttn
500 µm
a
Na-Am
Ca-Am
Chl
Ep
Chl + Ttn + Qtz
Na-Am
Ab
Cpx
500 µm
b
Ca-Am
Na-Am
Chl
15 µm
Cpx
Na-Am
Ca-Am
Sp
Na-Am + Ca-Am + Chl + Ep
250 µm
c
Na-Am + Ca-Am
Ep
Chl
Ab
250 µm
d
Ca-Am
Na-Am
Czo
Lws
Ab
Qtz
Na-Am
Chl
Ttn
60 µm
e
Sp
Na-Am
Ca-Am
Ab
Ttn
Chl
50 µm
f

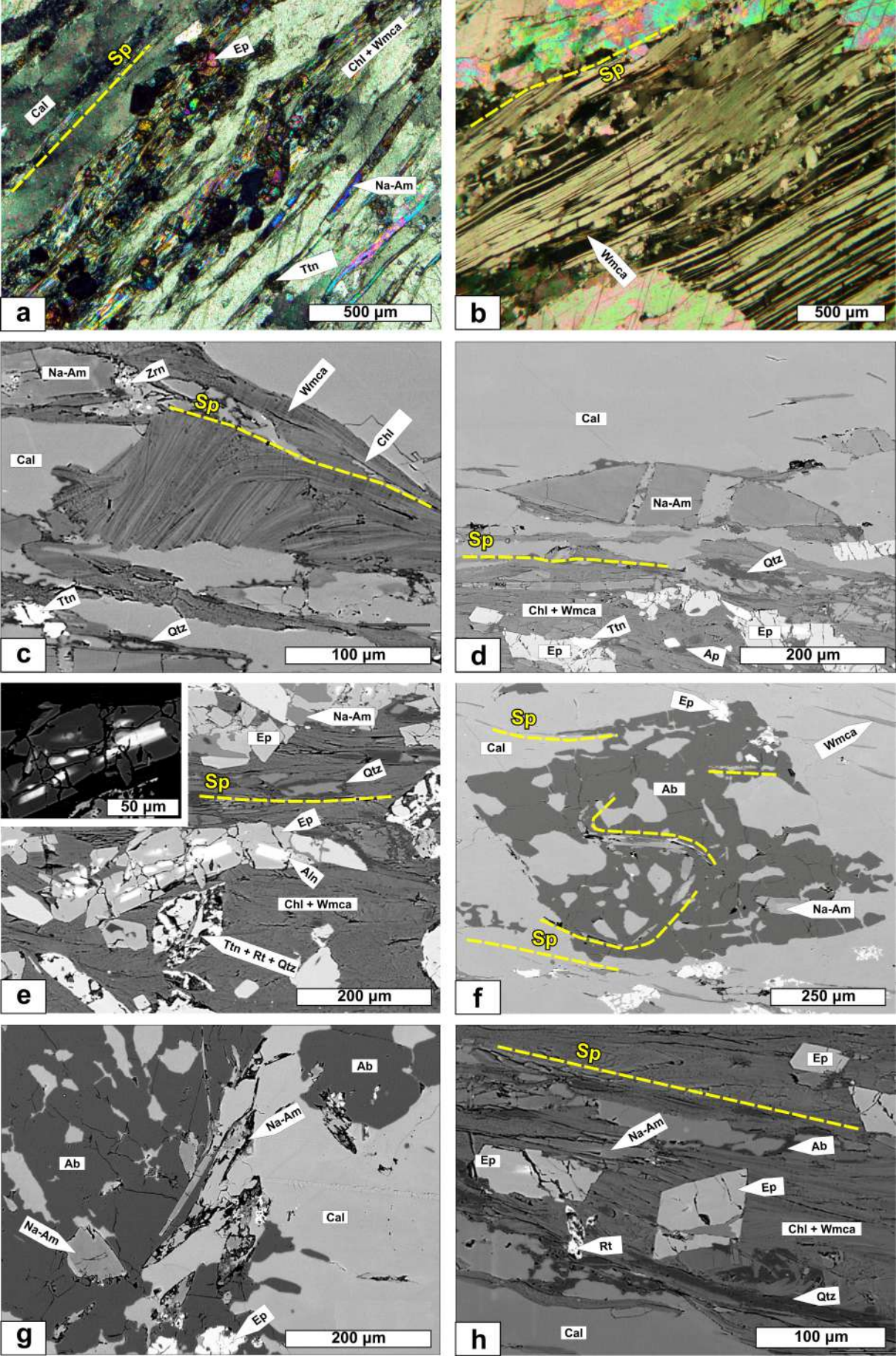
Sp
Ep
Chl + Wmca
Cal
Na-Am
Ttn
500 µm
a
Sp
Wmca
500 µm
b
Na-Am
Zrn
Wmca
Sp
Chl
Cal
Ttn
Qtz
100 µm
c
Cal
Na-Am
Sp
Qtz
Chl + Wmca
Ttn
Ep
Ep
Ap
200 µm
d
50 µm
Na-Am
Ep
Qtz
Sp
Ep
Aln
Chl + Wmca
Ttn + Rt + Qtz
200 µm
e
Sp
Ep
Cal
Wmca
Ab
Na-Am
Sp
250 µm
f
Ab
Na-Am
Ab
Cal
Na-Am
Ep
200 µm
g
Sp
Ep
Na-Am
Ab
Ep
Ep
Chl + Wmca
Rt
Qtz
Cal
100 µm
h

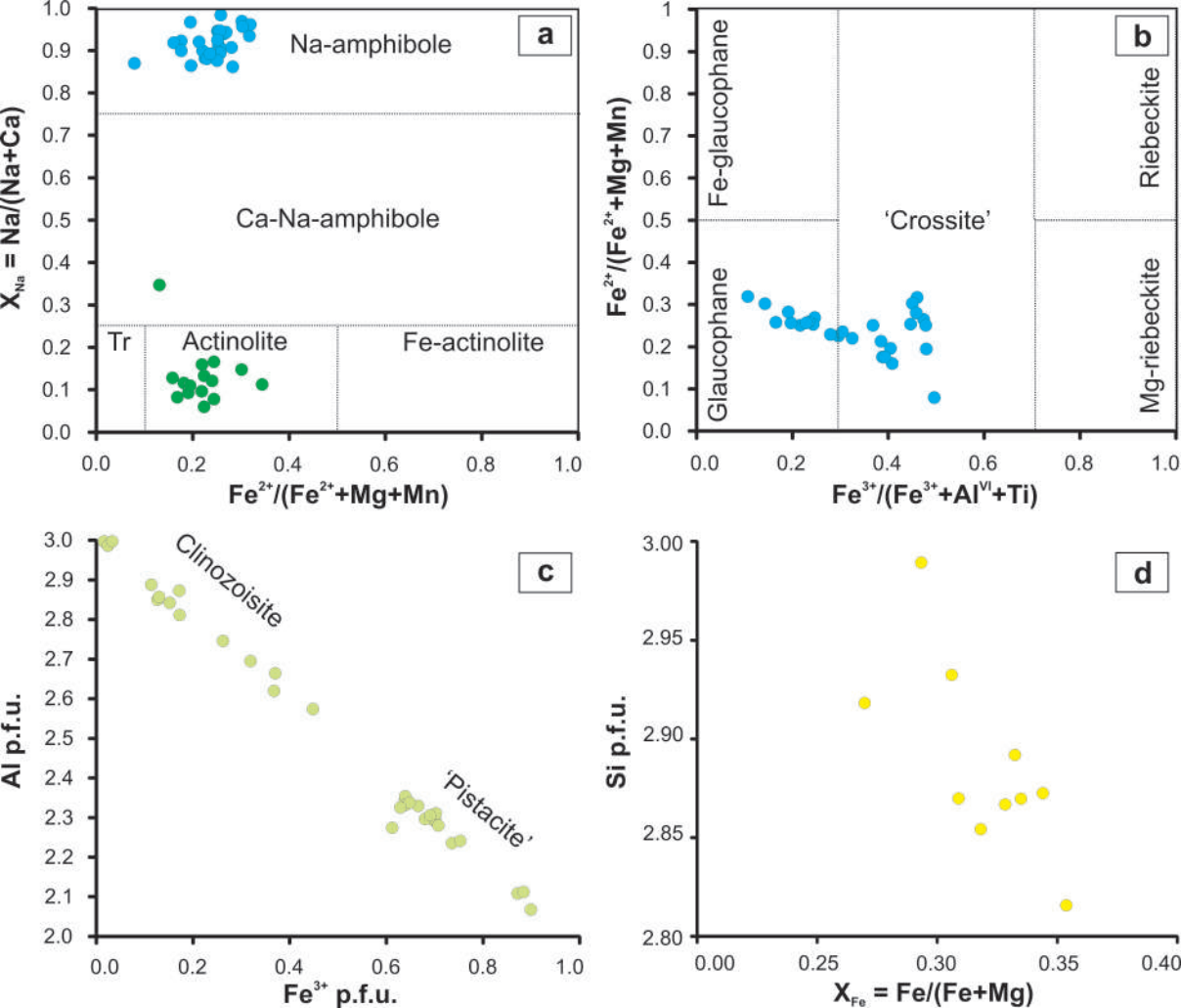
a
Na-amphibole
Ca-Na-amphibole
Tr
Actinolite
Fe-actinolite
X_{Na} = Na/(Na+Ca)
$Fe^{2+}/(Fe^{2+}+Mg+Mn)$
b
Fe-glaucophane
Riebeckite
'Crossite'
Glaucophane
Mg-riebeckite
$Fe^{2+}/(Fe^{2+}+Mg+Mn)$
$Fe^{3+}/(Fe^{3+}+Al^{VI}+Ti)$
c
Clinozoisite
'Pistacite'
Al p.f.u.
Fe^{3+} p.f.u.
d
Si p.f.u.
X_{Fe} = Fe/(Fe+Mg)

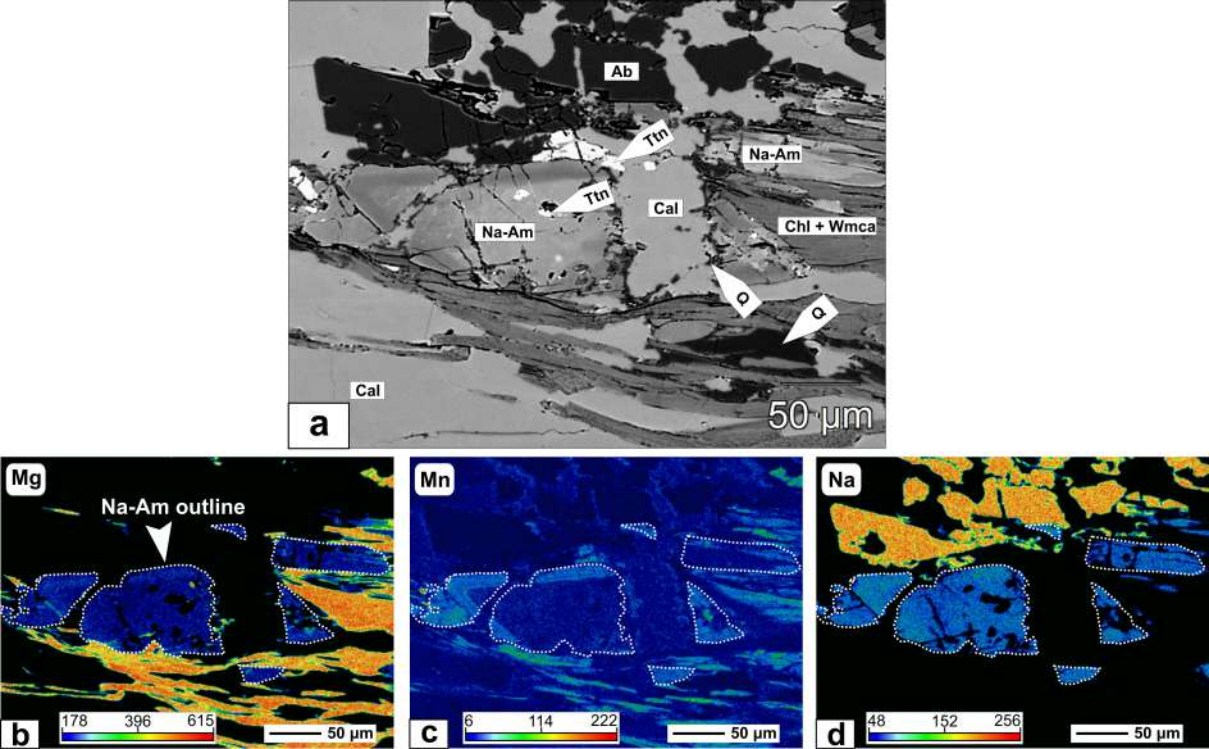
Ab
Ttn
Ttn
Na-Am
Cal
Na-Am
Chl + Wmca
p
q
Cal
a
50 µm
Mg
Na-Am outline
178
396
615
50 µm
b
Mn
6
114
222
50 µm
c
Na
48
152
256
50 µm
d

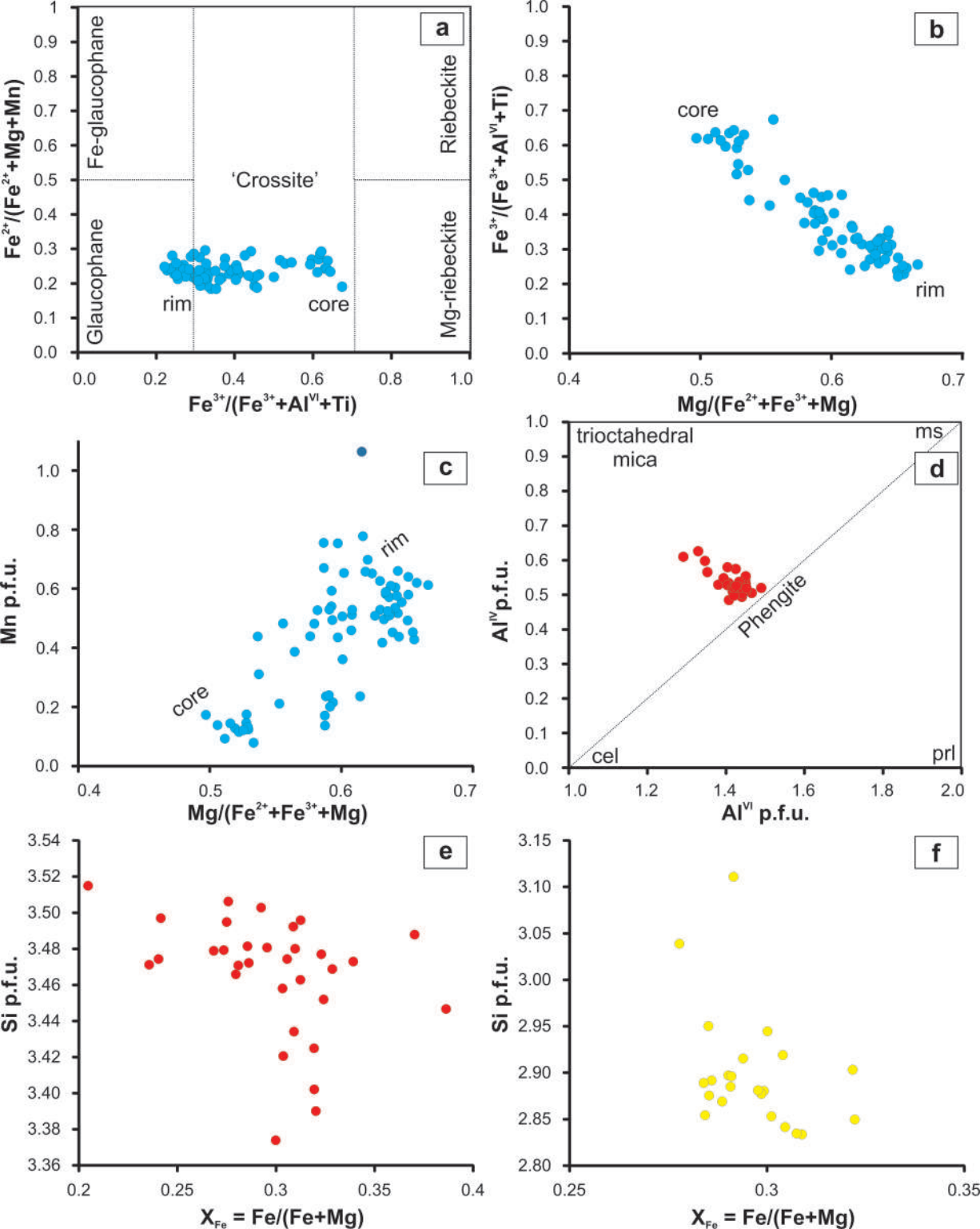
a
Fe-glaucophane
Riebeckite
'Crossite'
Glaucophane
Mg-riebeckite
rim
core
Fe2+/(Fe2+ +Mg+Mn)
Fe3+/(Fe3+ +AlVI+Ti)
b
core
rim
Fe3+/(Fe3+ +AlVI+Ti)
Mg/(Fe2+ +Fe3+ +Mg)
c
rim
core
Mn p.f.u.
Mg/(Fe2+ +Fe3+ +Mg)
d
trioctahedral
mica
ms
Phengite
cel
prl
AlIV p.f.u.
AlVI p.f.u.
e
Si p.f.u.
XFe = Fe/(Fe+Mg)
f
Si p.f.u.
XFe = Fe/(Fe+Mg)

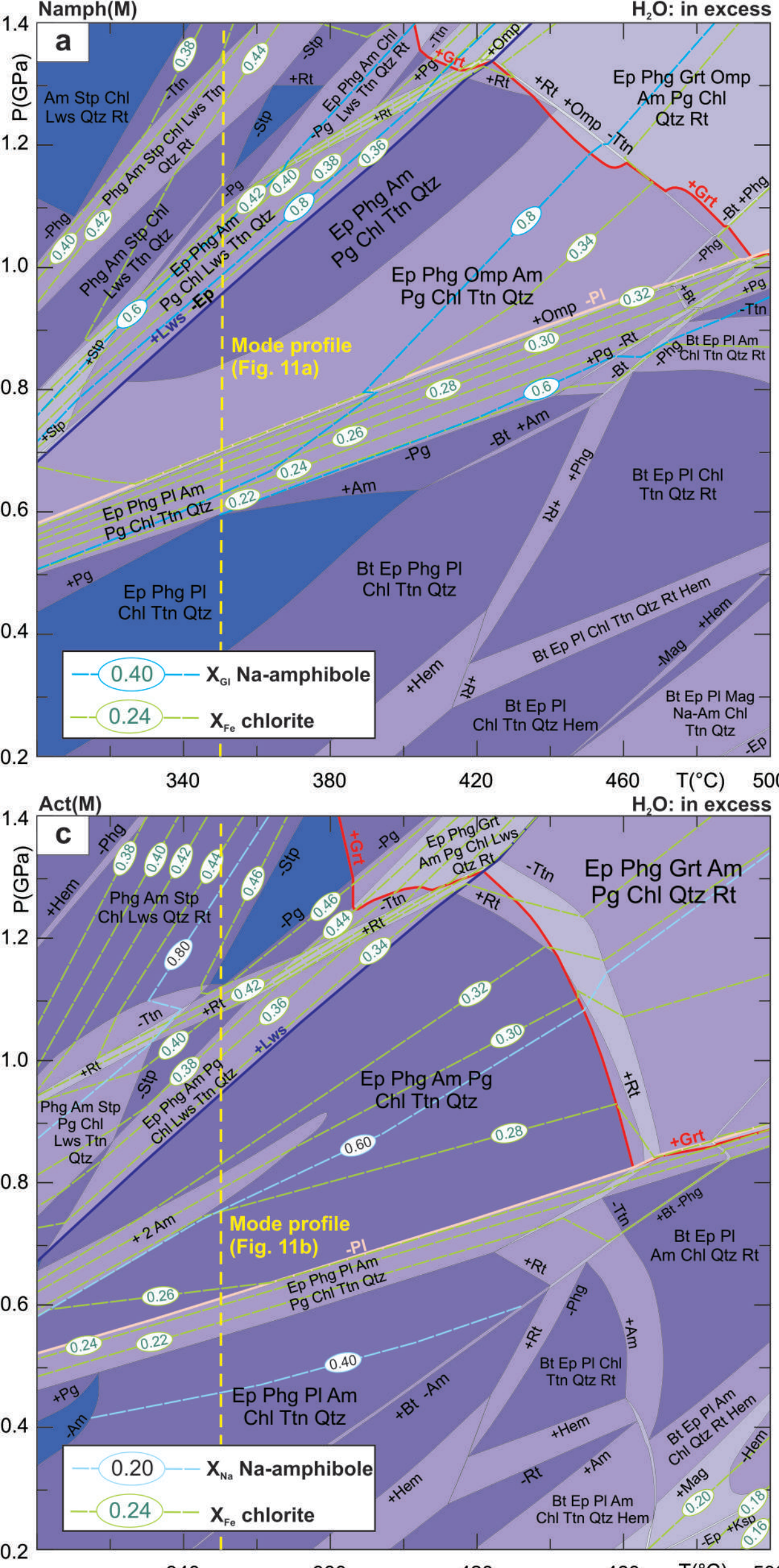
a
Namph(M)
H2O: in excess
P(GPa)
T(°C)
Am Stp Chl Lws Qtz Rt
Phg Am Stp Chl Lws Qtz Rt
Ep Phg Am Chl Lws Ttn Qtz Rt
Ep Phg Am Pg Chl Lws Ttn Qtz
Ep Phg Am Pg Chl Ttn Qtz
Ep Phg Grt Omp Am Pg Chl Qtz Rt
Ep Phg Omp Am Pg Chl Ttn Qtz
Mode profile (Fig. 11a)
Ep Phg Pl Am Pg Chl Ttn Qtz
Ep Phg Pl Chl Ttn Qtz
Bt Ep Phg Pl Chl Ttn Qtz
Bt Ep Pl Chl Ttn Qtz Rt
Bt Ep Pl Chl Ttn Qtz Rt Hem
Bt Ep Pl Chl Ttn Qtz Hem
Bt Ep Pl Mag Na-Am Chl Ttn Qtz
Bt Ep Pl Chl Ttn Qtz Rt
Bt Ep Pl Am Chl Ttn Qtz Rt
0.40 XGl Na-amphibole
0.24 XFe chlorite
b
Lawsonite + amphibole blueschists
Lawsonite + amphibole + paragonite
Epidote + amphibole + paragonite blueschists
Epidote + amphibole + omphacite + paragonite
Epidote + amphibole + albite + paragonite
Epidote + amphibole + albite
Epidote + paragonite + albite
Albite + Epidote greenschists
Garnet-bearing fields
c
Act(M)
Phg Am Stp Chl Lws Qtz Rt
Ep Phg Grt Am Pg Chl Lws Qtz Rt
Ep Phg Grt Am Pg Chl Qtz Rt
Ep Phg Am Pg Chl Ttn Qtz
Phg Am Stp Pg Chl Lws Ttn Qtz
Mode profile (Fig. 11b)
Ep Phg Pl Am Pg Chl Ttn Qtz
Ep Phg Pl Am Chl Ttn Qtz
Bt Ep Pl Am Chl Qtz Rt
Bt Ep Pl Chl Ttn Qtz Rt
Bt Ep Pl Am Chl Qtz Rt Hem
Bt Ep Pl Am Chl Ttn Qtz Hem
0.20 XNa Na-amphibole
0.24 XFe chlorite
d
Lawsonite + amphibole blueschists
Lawsonite + amphibole + paragonite
Epidote + amphibole + paragonite blueschists
Epidote + paragonite + albite
Epidote + amphibole + albite + paragonite
Epidote + amphibole + albite greenschists
Epidote + albite greenschists
Garnet-bearing fields

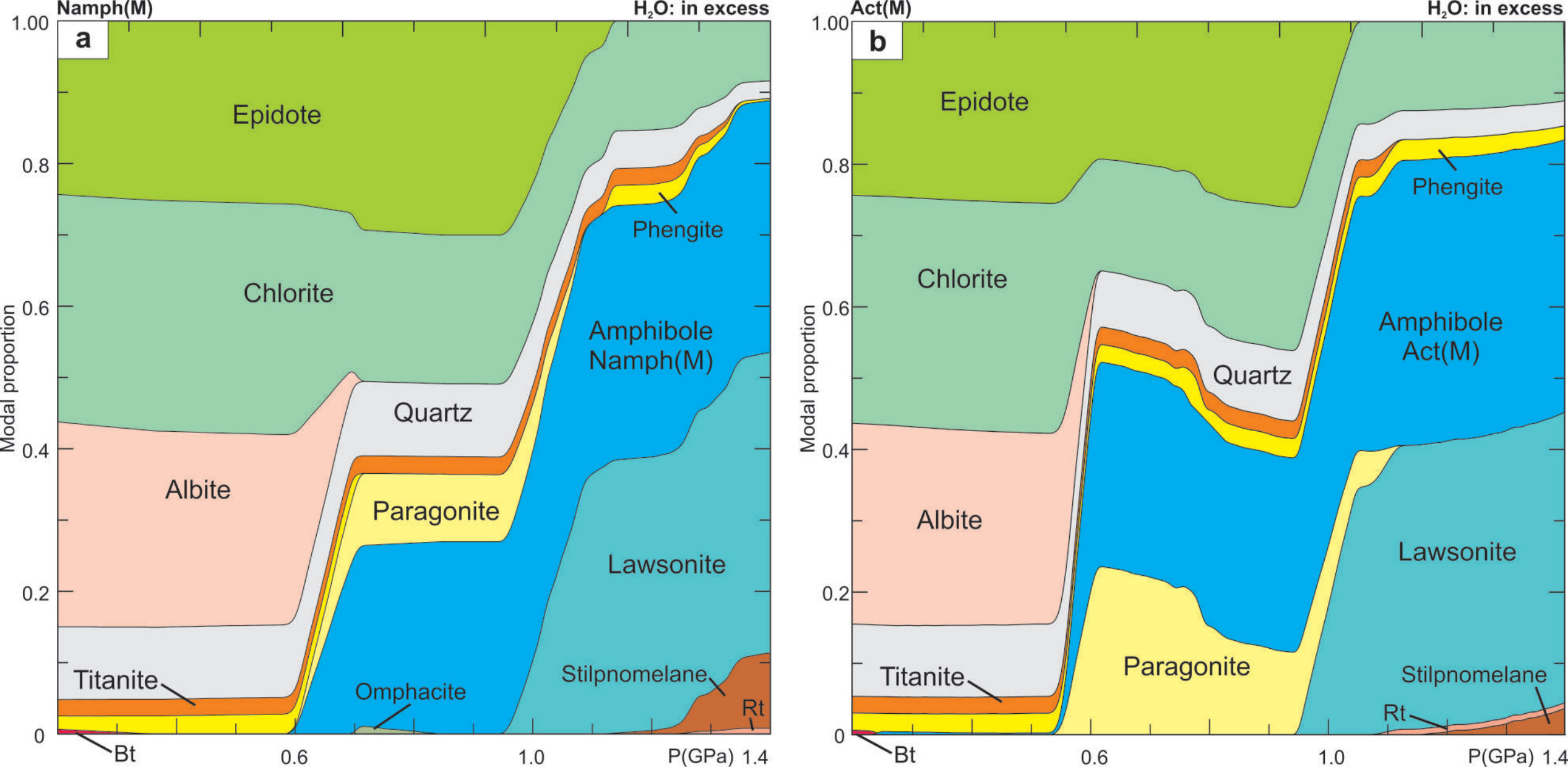
Namph(M)
H2O: in excess
a
Epidote
Chlorite
Albite
Titanite
Bt
Phengite
Amphibole
Namph(M)
Quartz
Paragonite
Omphacite
Lawsonite
Stilpnomelane
Rt
Modal proportion
1.00
0.8
0.6
0.4
0.2
0
0.6
1.0
P(GPa) 1.4
Act(M)
H2O: in excess
b
Epidote
Chlorite
Albite
Titanite
Bt
Phengite
Amphibole
Act(M)
Quartz
Paragonite
Lawsonite
Stilpnomelane
Rt
Modal proportion
1.00
0.8
0.6
0.4
0.2
0
0.6
1.0
P(GPa) 1.4

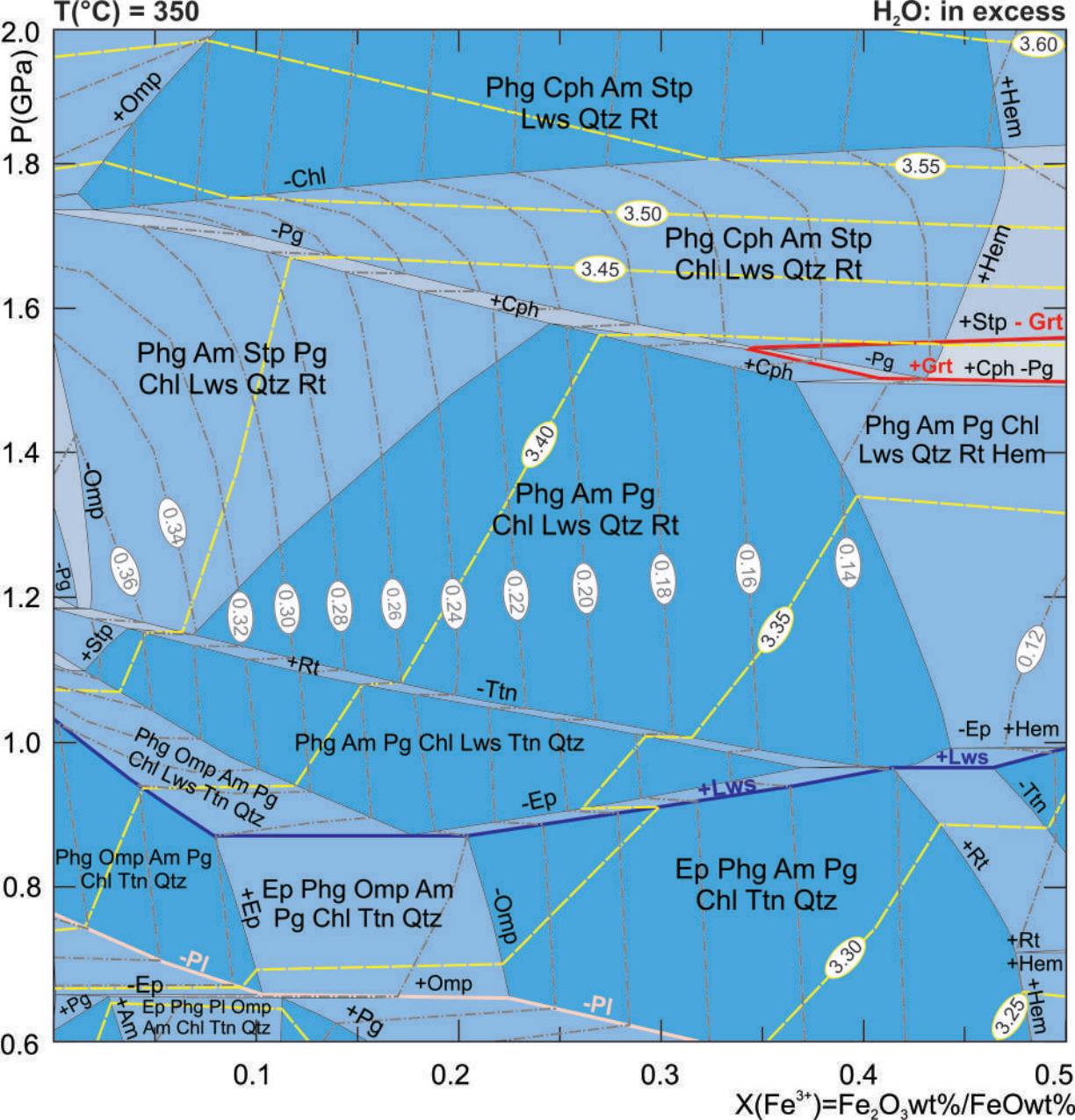
T(°C) = 350
H2O: in excess
P(GPa)
2.0
1.8
1.6
1.4
1.2
1.0
0.8
0.6
0.1
0.2
0.3
0.4
0.5
X(Fe3+)=Fe2O3wt%/FeOwt%
Phg Cph Am Stp Lws Qtz Rt
Phg Cph Am Stp Chl Lws Qtz Rt
Phg Am Stp Pg Chl Lws Qtz Rt
Phg Am Pg Chl Lws Qtz Rt
Phg Am Pg Chl Lws Qtz Rt Hem
Phg Am Pg Chl Lws Ttn Qtz
Phg Omp Am Pg Chl Lws Ttn Qtz
Phg Omp Am Pg Chl Ttn Qtz
+Ep Phg Omp Am Pg Chl Ttn Qtz
Ep Phg Am Pg Chl Ttn Qtz
Ep Phg Pl Omp Am Chl Ttn Qtz
+Omp
-Chl
-Pg
+Cph
+Stp - Grt
-Pg +Grt +Cph -Pg
+Hem
-Omp
+Stp
+Rt
-Ttn
-Ep +Hem
+Lws
-Ep
-Pl
+Pg
+Am
3.60
3.55
3.50
3.45
3.40
3.35
3.30
3.25
0.34
0.36
0.32
0.30
0.28
0.26
0.24
0.22
0.20
0.18
0.16
0.14
0.12

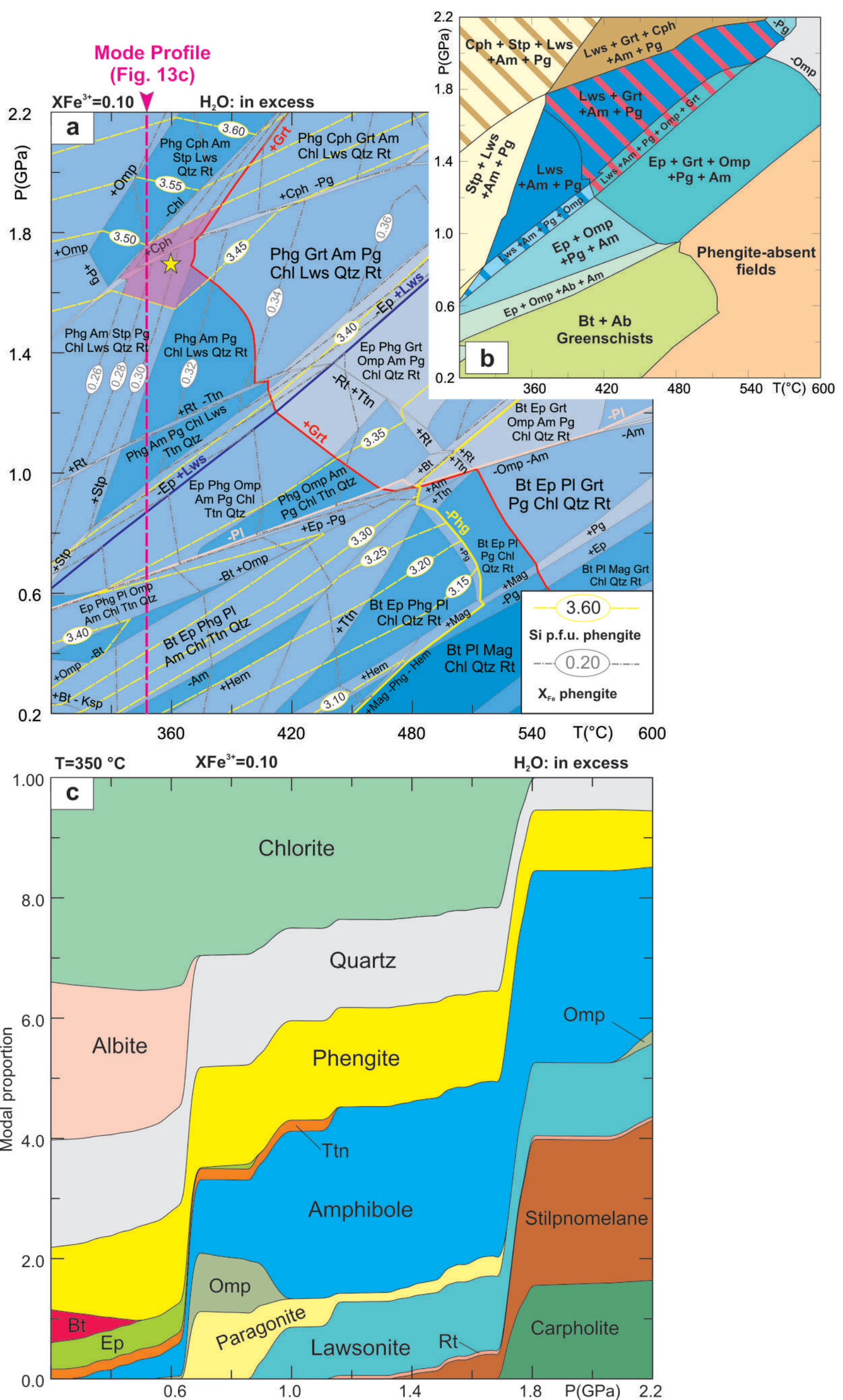
Mode Profile
(Fig. 13c)
XFe3+=0.10
H2O: in excess
a
P(GPa)
T(°C)
Phg Cph Am Stp Lws Qtz Rt
Phg Cph Grt Am Chl Lws Qtz Rt
Phg Grt Am Pg Chl Lws Qtz Rt
Phg Am Stp Pg Chl Lws Qtz Rt
Phg Am Pg Chl Lws Qtz Rt
Ep Phg Grt Omp Am Pg Chl Qtz Rt
Phg Am Pg Chl Lws Ttn Qtz
Ep Phg Omp Am Pg Chl Ttn Qtz
Phg Omp Am Pg Chl Ttn Qtz
Bt Ep Grt Omp Am Pg Chl Qtz Rt
Bt Ep Pl Grt Pg Chl Qtz Rt
Bt Ep Pl Pg Chl Qtz Rt
Bt Pl Mag Grt Chl Qtz Rt
Ep Phg Pl Omp Am Chl Ttn Qtz
Bt Ep Phg Pl Am Chl Ttn Qtz
Bt Ep Phg Pl Chl Qtz Rt
Bt Pl Mag Chl Qtz Rt
3.60
Si p.f.u. phengite
0.20
XFe phengite
b
Cph + Stp + Lws +Am + Pg
Lws + Grt + Cph +Am + Pg
Lws + Grt +Am + Pg
Stp + Lws +Am + Pg
Lws +Am + Pg
Ep + Grt + Omp +Pg + Am
Ep + Omp +Pg + Am
Phengite-absent fields
Ep + Omp +Ab + Am
Bt + Ab Greenschists
T=350 °C
XFe3+=0.10
H2O: in excess
c
Modal proportion
P(GPa)
Chlorite
Quartz
Albite
Phengite
Omp
Ttn
Amphibole
Stilpnomelane
Bt
Ep
Paragonite
Lawsonite
Rt
Carpholite

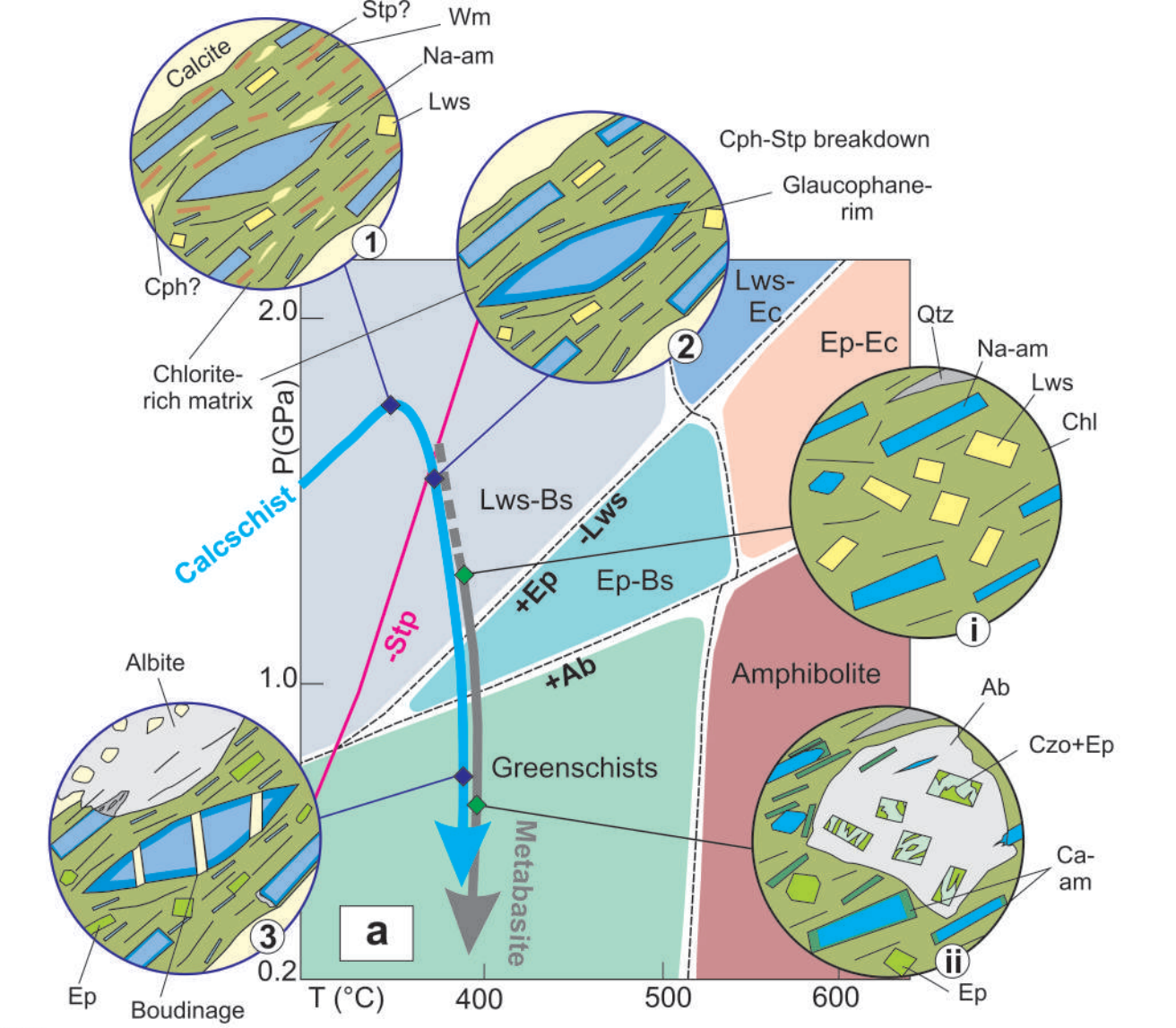
Stp?
Wm
Na-am
Lws
Calcite
Cph-Stp breakdown
Glaucophane-rim
Cph?
Chlorite-rich matrix
Lws-Ec
Ep-Ec
Qtz
Na-am
Lws
Chl
2.0
P(GPa)
Calcschist
Lws-Bs
-Lws
+Ep
Ep-Bs
-Stp
+Ab
Amphibolite
Albite
1.0
Ab
Czo+Ep
Greenschists
Metabasite
Ca-am
a
0.2
Ep
Boudinage
T (°C)
400
500
600
Ep

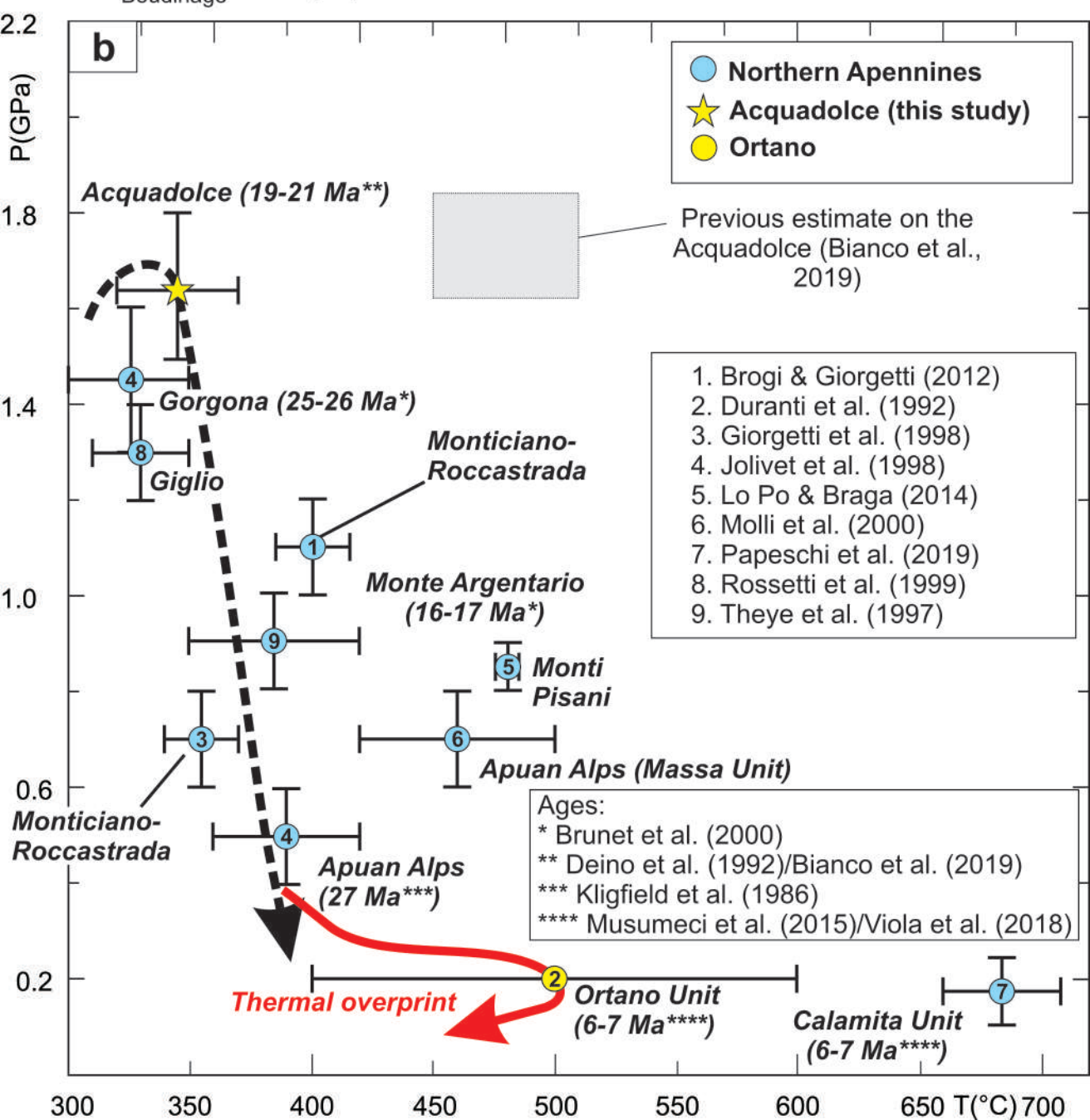
b
Northern Apennines
Acquadolce (this study)
Ortano
2.2
P(GPa)
Acquadolce (19-21 Ma**)
1.8
Previous estimate on the Acquadolce (Bianco et al., 2019)
1. Brogi & Giorgetti (2012)
2. Duranti et al. (1992)
3. Giorgetti et al. (1998)
4. Jolivet et al. (1998)
5. Lo Po & Braga (2014)
6. Molli et al. (2000)
7. Papeschi et al. (2019)
8. Rossetti et al. (1999)
9. Theye et al. (1997)
1.4
Gorgona (25-26 Ma*)
Monticiano-Roccastrada
Giglio
Monte Argentario (16-17 Ma*)
1.0
Monti Pisani
Apuan Alps (Massa Unit)
0.6
Monticiano-Roccastrada
Apuan Alps (27 Ma***)
Ages:
* Brunet et al. (2000)
** Deino et al. (1992)/Bianco et al. (2019)
*** Kligfield et al. (1986)
**** Musumeci et al. (2015)/Viola et al. (2018)
0.2
Thermal overprint
Ortano Unit (6-7 Ma****)
Calamita Unit (6-7 Ma****)
300
350
400
450
500
550
600
650
T(°C)
700